

# **POINT SPREAD FUNCTION(PSF) PHOTOMETRY USING POLAR SHAPELETS TECHNIQUE FOR WALOP**

*A report Submitted  
for semester VI Project*

*by*

**SHRISH**

*in supervision of*

**DR. TUHIN GHOSH AND PROF. A. N. RAMAPRAKASH**



*to the*

**School of Physical Sciences**

**National Institute of Science Education and Research**

**Bhubaneswar**

## ABSTRACT

Our knowledge about the universe has trickled down from the sky in the form of photons in all spectrums. High accuracy photometry has been always challenging for astronomers. Many excellent techniques have been developed to meet the challenge. The point spread function(PSF) photometry, a technique of stellar photometry(counting photons from stars), is widely used for high accuracy measurements.

Pasiphae survey, one of its kind plans to scan a large part of the sky to measure starlight polarization in the optical region with help of an instrument, Wide Area Linear Optical Polarimeter(WALOP).

Every optical instrument is anisotropic to some extent that introduces further polarization, needed to tackle beforehand. Measurement of polarization has evolved into a separate challenge, as we are dealing with a very low degree of polarization ( $\leq 0.2\%$ ). The WALOP polarimeter plans to measure polarization up to  $p = 0.2\%$  of stars brighter than  $R = 16.5$  magnitude with a sensitivity in  $p$  of  $\leq 0.1\%$ . Unprecedented high accuracy stellar photometry( $error \leq 0.07\%$ ) is required for the goal.

In this project, We have studied PSF photometry with an analytical PSF model using polar shapelets, an orthogonal and complete basis for 2D images. We have studied their applicability and accuracy limits for our project.

# Contents

<b>1</b>	<b>Introduction and Background</b>	<b>1</b>
1.1	Introductions . . . . .	1
1.2	Stokes Parameters . . . . .	2
1.3	Four Channel Polarimeter . . . . .	3
1.4	RoboPol . . . . .	3
1.5	Our Instrument: WALOP . . . . .	4
<b>2</b>	<b>PSF modeling For WALOP Output From Zemax Simulations</b>	<b>8</b>
2.1	Photometry . . . . .	8
2.1.1	Stellar Photometry . . . . .	8
2.1.2	Point Spread Functions . . . . .	8
2.1.3	Aperture Photometry . . . . .	8
2.1.4	PSF Photometry . . . . .	11
2.2	PSF Modeling For WALOP . . . . .	13
2.2.1	Available Module and Error Analysis . . . . .	13
2.2.2	Analytical Model . . . . .	15
<b>3</b>	<b>PSF modeling For WALOP Output Using Polar Shapelets</b>	<b>21</b>
3.1	Polar Shapelets . . . . .	21
3.2	Star Specifications . . . . .	22
3.3	Zemax Input Images . . . . .	24
3.4	Processing Zemax Output Images . . . . .	25
3.5	Exposure Time Analysis . . . . .	25
3.6	Steps Taken for PSF Modeling . . . . .	26
3.7	Results . . . . .	26
<b>4</b>	<b>Photometry Error Analysis</b>	<b>29</b>
4.1	PSF Photometry Error . . . . .	29
4.2	Polar Shapelets PSF Photometry . . . . .	30
4.3	Error Analysis . . . . .	31
<b>5</b>	<b>Other Possible Applications of Shapelets Analysis</b>	<b>33</b>
5.1	Image Components . . . . .	33
5.2	Application in Image Recognition . . . . .	33
5.3	Steps Taken . . . . .	34
5.4	Results . . . . .	36
<b>References</b>		<b>38</b>

# List of Figures

1.1	Polarized dust emission and polarization of transmitted light both result from the alignment of the dust grain's short axis with the direction of the magnetic field. . . . .	1
1.2	Measuring Stokes parameters using simple polarizer.[1] . . . . .	3
1.3	Schematic of the half-wave plate ( $\lambda/2$ ) and Wollaston prism (WP) system of RoboPol. The fast optical axes of the elements are shown with bidirectional arrows. The angle of the axis, $\theta$ , is denoted below each half-wave plate. . . . .	3
1.4	(Up) Optical design of WALOP (side view) Unlike Robopol here images are being produced on four different CCD. . . . .	6
1.5	(Down) Optical design of WALOP (side view) preliminary schematics.[4] . . . . .	6
1.6	4-beams on 4-CCDs . . . . .	7
2.1	Finding an optimum aperture radius for aperture photometry with the growth curve analysis. . . . .	9
2.2	Aperture photometry of a background subtracted star. Signal by noise ratio decreases with increase of aperture radius. For white aperture Radius=6 pixel, Signal flux=1854.74, Noise=53.17 ,and S/N=34.88. For Red aperture Radius=14 pixel, Signal flux=2090.32, Noise=124.07 ,and S/N=16.84. For Blue aperture Radius=14 pixel, Signal flux = 2195.85 Noise= 159.52 and S/N = 13.76. . . . .	10
2.3	Getting contamination from the nearby galaxy while doing aperture photometry of a star(SN). . . . .	11
2.4	Crowded field. Brighter star shadow fainter star giving a tough time for aperture photometry. Overlapped stars can not be handled with aperture photometry. . . . .	12
2.5	A typical PSF. . . . .	12
2.6	Some WALOP PSFs at a different field of view (for worst-case). . . . .	13
2.7	Some good star cutouts in $30 \times 30$ pixels from the best case ZEMAX output. . . . .	15
2.8	Error analysis of the PSF photometry by Photutils with the best case of Zemax output. . . . .	16
2.9	Error analysis of the PSF photometry by Photutils with the worst case of Zemax output. . . . .	16
2.10	The first 21 Zernike polynomials( $Z_n^m$ ) in unit disk. Where n is the radial degree and m is the azimuthal degree. . . . .	17
2.11	Some typical PSFs made from Zernike Polynomials. Left: $p = 2.0$ , $b_{2,0} = 0.1$ , $b_{1,-1} = 0.04$ , and $b_{2,-2} = 0.04$ . Right: $p = 2.0$ , $b_{2,0} = 0.1$ , $b_{1,-1} = 0.036$ , and $b_{2,-2} = 0.065$ . . . . .	18
2.12	Left: $p = 2.0$ , $b_{2,0} = 0.1$ , $b_{1,-1} = 0.007$ , $b_{1,1} = 0.12$ and $b_{4,2} = 0.04$ . Right: $p = 2.0$ , $b_{2,0} = 0.1$ , $b_{1,-1} = 0.007$ , $b_{1,1} = 0.13$ and $b_{4,2} = 0.04$ . See how unstable the PSF is with respect to the parameter $b_{1,1}$ . . . . .	18
2.13	Some random star cutouts fitted with elliptical Gaussian. Top: $\sigma_x = 3.620$ , $\sigma_y = 4.598$ and $\sigma_{xy} = -0.038$ with $I_o = 1.0$ . Bottom : $\sigma_x = 3.315$ , $\sigma_y = 4.167$ and $\sigma_{xy} = -0.023$ . . . . .	20
3.1	The real part of the polar shapelets (for $\beta = 2.1$ ) and different combinations of $n$ and $m$ values. Each image is plotted for x and y axis form $-8$ to $8$ , colorbar represents the numerical value of the polar shapelet. . . . .	23
3.2	A small part of a input image with random stars. . . . .	24
3.3	Trace of required exposure time to achieve various error tolerance. . . . .	25
3.4	Histogram of photometric error in PSF modeling(For 1000 random star points on CCD). . . . .	27

3.5	Some random star cutouts fitted with polar shapelets. The residuals are uncorrelated with the input PSF. X and Y at the top of the plots represent the PSF location on the CCD plane. Each image is plotted for x and y axis from -8 to 8, colorbar represents the photon counts.	28
4.1	1D Gaussian fitted with flux data.	30
4.2	1D Gaussian fitted with flux data.	31
4.3	Left: Percentage error of PSF photometry on CCD. Right: Histogram of percentage error of PSF photometry of 400 stars.	32
5.1	Recovering a black and white image of a puppy with polar shapelets analysis. It just needed 20 polar shapelets with a total of 231 components.	33
5.2	Component analysis of a low resolution black and white cat image( $100 \times 100$ pixels) with 20 polar shapelets .	34
5.3	Some sample image of cats from the datasets.	35
5.4	Some sample image of dogs from the datasets.	35
5.5	Some sample image of pandas from the datasets.	36
5.6	Confusion matrix for predicted class by the Random Forest Classifier. Element $[i, j]$ represent number on instance algorithm confused $i^{th}$ label for $j$ . For example element $[1, 2]$ is number of cases algorithm confused a cat for a dog	37

# Chapter 1

## Introduction and Background

### 1.1 Introductions

Starlight polarization gives information about the interstellar magnetic field (ISM) that lies between the star and the observer. The polarization angle( $\theta$ ), can give us the direction of the magnetic field component on the sky plane. Measurement of the degree of linear polarization( $p$ ) validates the angle measurement. Through polarization data with given distance information for stars, we can know a lot about the ISM magnetic field.

Measuring precisely the polarization state of stars (Stokes parameters i.e  $q$  and  $u$ ) can aid in ongoing efforts to model the 3D Galactic magnetic field(called tomography). 3D tomography of the magnetic field can have paramount importance in detecting B-mode polarization of Cosmic Microwave Background (CMB). B-mode polarization of CMB is said to be the signature of the gravitational wave of the big bang on microwave radiation. This will help in providing experimental proof for Big-Bang theory.[5]

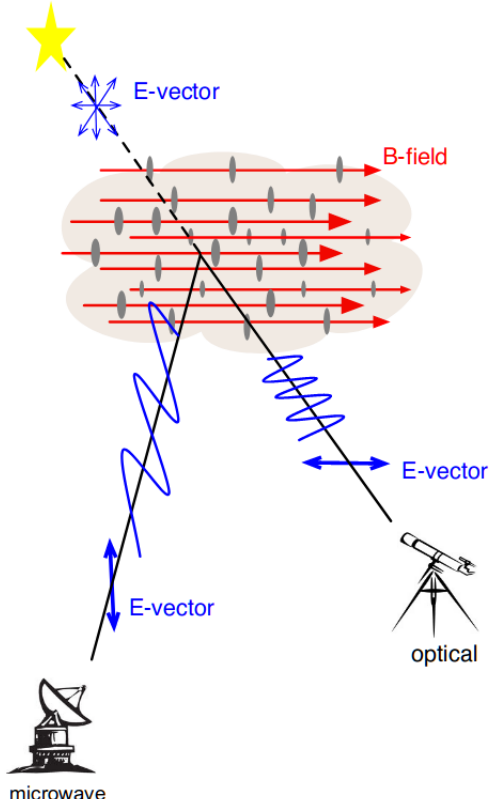


Figure 1.1: Polarized dust emission and polarization of transmitted light both result from the alignment of the dust grain's short axis with the direction of the magnetic field.

Starlight is intrinsically unpolarized. When it passes through a dust cloud, however, some of it gets selectively absorbed, and the fraction that emerges is partially linearly polarized. This polarization happens due to the alignment of dust grains' shorter axis along the magnetic field, which also causes the polarization of dust emission. Dust absorption preferentially attenuates the component of the electric field of starlight along the long axis of the aspherical dust grains. The transmitted light is thus partially polarized to the shorter axis (along the magnetic field, see in figure 1.1). Emission and absorption by the same population of dust grains thus traces back the same magnetic field, and the polarization of emitted and transmitted light will be orthogonal to each other.

If we have the polarization data for large numbers of stars with given distances, we could deduce the 3D structure of the magnetic field in the interstellar medium in between these stars.

Measuring starlight polarization ( $p \leq 2\%$ ) is a very delicate experiment. The instrument which is being used to measure polarization is a four-channel imaging polarimeter (see in figure 1.3), which uses two half-wave plates and two Wollaston prisms to simultaneously measure the relative Stokes parameters  $q = Q/I$  and  $u = U/I$  ( $I$  is the total intensity and  $Q, U$  are the absolute Stokes parameters). Optical instruments can also have anisotropy of itself which introduces further polarization to the starlight. That is needed to be corrected by an instrumental model for the spatial and the intensity part.

## 1.2 Stokes Parameters

The Stokes parameters are a set of values that describe the polarization state of all kinds of electromagnetic radiation defined by George Gabriel Stokes in 1852. Partially polarized and incoherent radiations are difficult to express using conventional polarization ellipse. Stokes parameters are a mathematically convenient alternative that expresses all aspects(total intensity ( $I$ ), degree of polarization ( $p$ ) and shape of polarization ellipses) using a single vector called Stokes vector.[1]

Unlike the conventional way of describing polarization state, Stokes parameters are directly measurable as they are related to intensities of light in a different plane of polarization. For measurement purposes Stokes parameters are defined as followings.

$$I = I_{0^\circ} + I_{90^\circ}, \quad (1.1)$$

$$Q = I_{0^\circ} - I_{90^\circ}, \quad (1.2)$$

$$U = I_{45^\circ} - I_{135^\circ}, \quad (1.3)$$

$$V = I_{RCP} - I_{LCP}, \quad (1.4)$$

here  $I_{angle}$  are intensity measures for the corresponding (angle with positive x axis) plane of polarization(see in figure 1.2).  $I_{RCP}$  and  $I_{LCP}$  are intensity measured for right circular and left circular polarization respectively. Intensity is measure of time averaged wave amplitude at position of detector.

The starlight is mainly polarized linearly; in general, circular polarization of light is rarely encountered in nature. So we focus only on measuring  $q (= \frac{Q}{I})$  and  $u (= \frac{U}{I})$ .

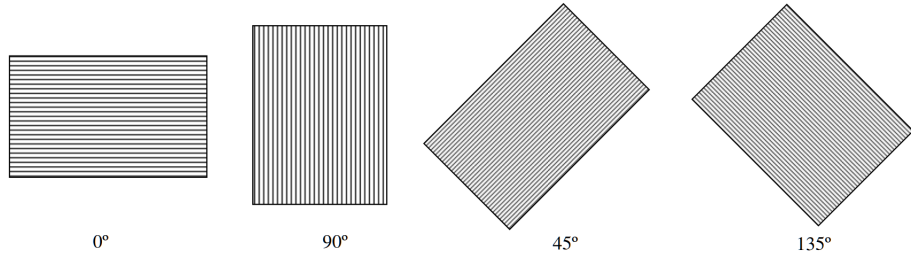


Figure 1.2: Measuring Stokes parameters using simple polarizer.[1]

### 1.3 Four Channel Polarimeter

The four-channel polarimeter uses a pair of Wollaston prisms (WP) as the beam analyzer to achieve simultaneous measurement of both Stokes  $Q$  and  $U$ . Four beams polarized at  $0^\circ$ ,  $45^\circ$ ,  $90^\circ$  and  $135^\circ$  emerge out of this prism pair. The measurement of the relative intensities of the first two beams provides the Stokes parameter  $Q$  ( $0^\circ, 90^\circ$ ) and relative intensities of the other two beams provides  $U(45^\circ, 135^\circ)$ . The prisms are placed in such a way that the telescope beam is shared approximately equally between the two, and all polarization states are imaged simultaneously at different positions on the detector(or on different detector).[4]

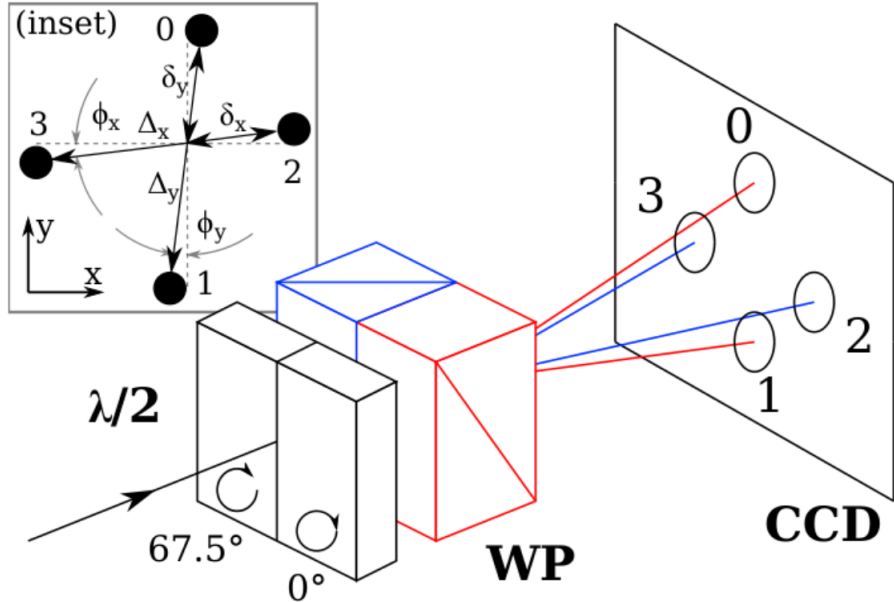


Figure 1.3: Schematic of the half-wave plate ( $\lambda/2$ ) and Wollaston prism (WP) system of RoboPol. The fast optical axes of the elements are shown with bidirectional arrows. The angle of the axis,  $\theta$ , is denoted below each half-wave plate.

### 1.4 RoboPol

RoboPol is a four-channel polarimeter, capable of measuring the linear stokes parameters in one exposure. A collimated telescope beam is shared equally by two quartz Wollaston

prisms, each with its half-wave plate in front (see in figure 1.3). Four beams of differing polarization states are output from this system and are imaged on a CCD detector (see in figure 1.3). Relative photometry of the four beam images provides the linear Stokes parameters. RoboPol is mounted on the 1.3 m telescope of the Skinakas Observatory in Crete, Greece.

It has no moving parts other than a filter wheel. Instead, as shown in figure 1.3, the instrument splits the pupil in two each half incident on a half-wave retarder followed by a Wollaston prism (WP). One prism is oriented such that it splits the rays falling on it in the horizontal plane (blue prism and rays in figure 1.3), while the other prism's orientation splits them in the vertical plane.

It uses the measured intensity of spots 0 and 1 (on the y-axis) to get Q for U it rotates wave by 135° by use of half-wave plate (spots 2 and 3). Additional 90° rotation is required to get spots on another axis(x-axis).

Every point in the sky is thereby projected to four points on the CCD. The fast axis of the half-wave retarder in front of the first prism is rotated by 67.5° with respect to the other retarder. In the instrument reference frame the horizontal channel measures the  $u = U/I$  fractional Stokes parameter, while the vertical channel measures the  $q = Q/I$  fractional Stokes parameter, simultaneously, with a single exposure. This design eliminates the need for multiple exposures with different half-wave plate positions, thereby avoiding systematic and random errors due to sky changes between measurements and imperfect alignment of rotating optical elements.

The expressions for the relative Stokes parameters and their uncertainties are

$$q = \frac{N_0 - N_1}{N_0 + N_1}, u = \frac{N_2 - N_3}{N_2 + N_3} \quad (1.5)$$

$$\sigma_q = \sqrt{\frac{4(N_1^2\sigma_0^2 + N_0^2\sigma_1^2)}{(N_0 + N_1)^4}}, \sigma_u = \sqrt{\frac{4(N_3^2\sigma_2^2 + N_2^2\sigma_3^2)}{(N_2 + N_3)^4}} \quad (1.6)$$

where  $N_0, N_1, N_2, N_3$  are the intensities of the upper, lower, right and left spots and  $\sigma_0, \sigma_1, \sigma_2, \sigma_3$  are their uncertainties. We estimate the uncertainty in a spot intensity  $\sigma_i$  following the method[4]

$$\sigma_i = \sqrt{N_i + \sigma_{sky}^2 A_{phot} + \frac{\sigma_{sky}^2 A_{phot}^2}{A_{sky}}} \quad (1.7)$$

where  $N_i$  is the spot intensity ,  $\sigma_{sky} = n_{sky}$  is the sky intensity (background) in a single pixel ,  $A_{phot}$  is the area (in pixels) of the photometry aperture, and  $A_{sky}$  is the area of the background estimation annulus. The first two terms account for counting statistics of the source and sky, while the third describes the uncertainty in the background estimation.

## 1.5 Our Instrument: WALOP

PASIPHAE (Polar Areas Stellar Imaging in Polarization High Accuracy Experiment) aims to map, with unprecedented accuracy, the polarization of millions of stars in areas of the sky

away from the galactic plane, in both the northern and the southern hemispheres. Combined with stellar distances provided by ESA's Gaia mission, this data will allow us, for the very first time, to construct a tomographic map of the Galactic magnetic field. Our ultimate goal: to clear the path towards the detection of the imprint of inflation on primordial light[6]. In order to perform the survey, a Wide Area Linear Optical Polarimeter(WALOP) is designed.

The WALOP polarimeter will implement a 4 channel, no moving parts, one-shot design, optimized for a wide field survey(see in figure 1.4,1.5). WALOP is an updated and highly sophisticated version of RoboPol. In the RoboPol polarimeter split angle was about  $1^\circ$  and WALOP a more sophisticated version has split angle of  $15^\circ$ . This enables us to produce one different CCD image for each intensity observation[5]. Although RoboPol had in principle wide-field capabilities, it was designed primarily for point source monitoring. For this reason, its sensitivity and accuracy are optimal for the central point source it observes. To minimize cost, all four spots in RoboPol are projected on the same CCD. This however in general reduces the sensitivity of the instrument, by projecting (at low  $p$  values) roughly a fourth of the photons of a point source against a full sky (since the sky is an extended source). This problem was solved by placing a mask at the center of the field of view, ensuring that each spot of the central point source is projected on a CCD region against only a quarter of the full sky intensity. However, field stars in RoboPol are measured against the full sky. The WALOP polarimeter will instead arrange for the four spots to fall on four different detectors, effectively extending the benefits of the RoboPol mask to the entire field. The instrument will thus have features uniquely appropriate for a wide field survey[5].

One polarimeter will be installed at the Skinakas 1.3 m telescope and the other at South African Astronomical Observatory(SAAO)'s 1m telescope. Both will have a field of view of  $30' \times 30'$  and will be able to measure the polarization of stars brighter than  $R = 16.5$  magnitude with a sensitivity in  $p$  of  $\leq 0.1\%$ .The instruments are currently under construction in IUCAA.

A survey of both northern and southern Galactic polar regions targeted by CMB experiments, covering over 10000 square degrees, which will measure linear optical polarization of over 360 stars per square degree (over 3.5 million stars, a 1000 fold increase over the state of the art) and deliver at least a  $3\sigma$  measurement for individual stars with polarization fraction ( $p = 0.5\%$ ). The survey will be conducted concurrently from the South African Astronomical Observatory in Sutherland, South Africa in the southern hemisphere, and the Skinakas Observatory in Crete, Greece, in the north.

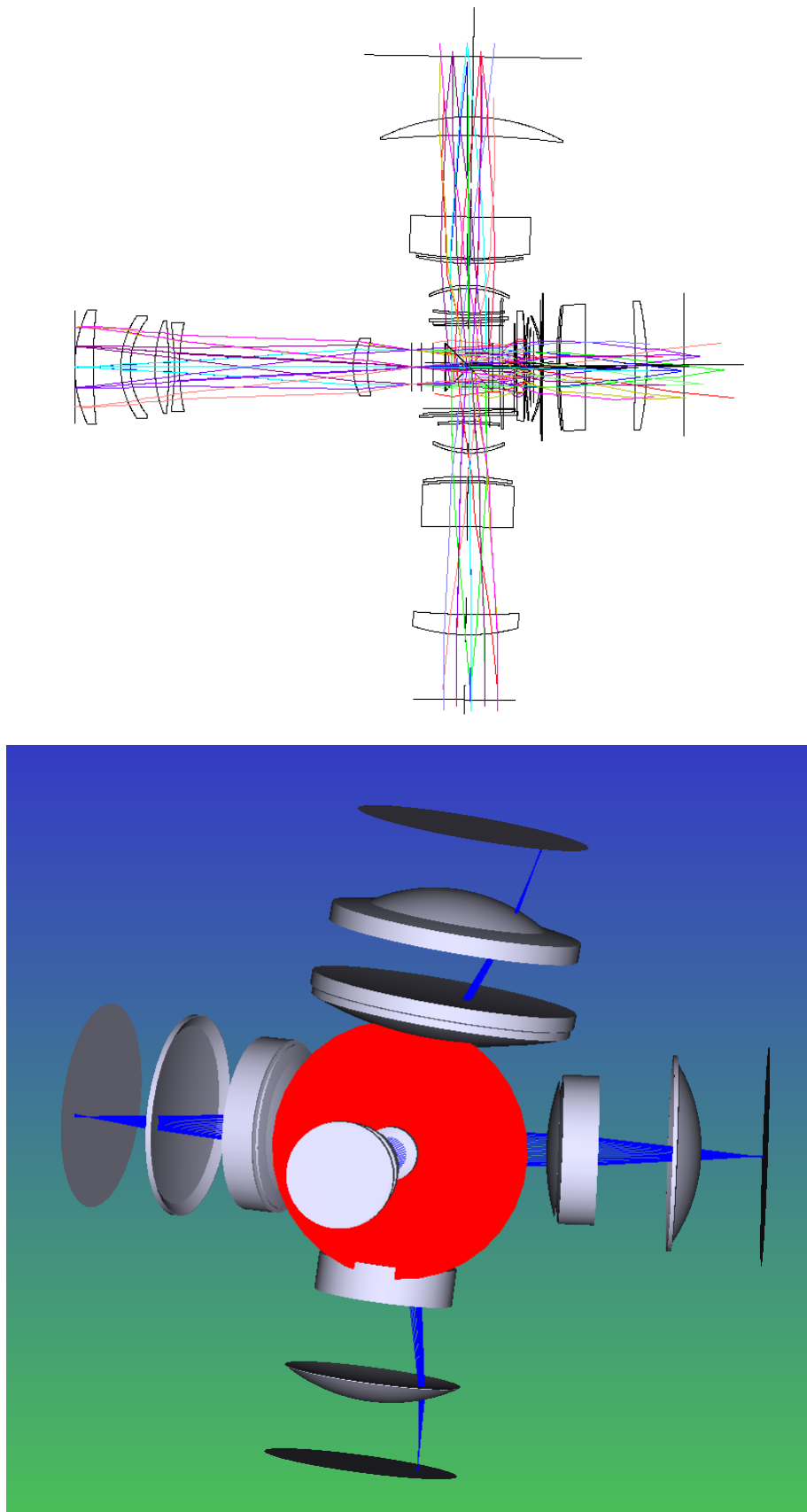


Figure 1.4: (Up) Optical design of WALOP (side view) Unlike Robopol here images are being produced on four different CCD.

Figure 1.5: (Down) Optical design of WALOP (side view) preliminary schematics.[4]

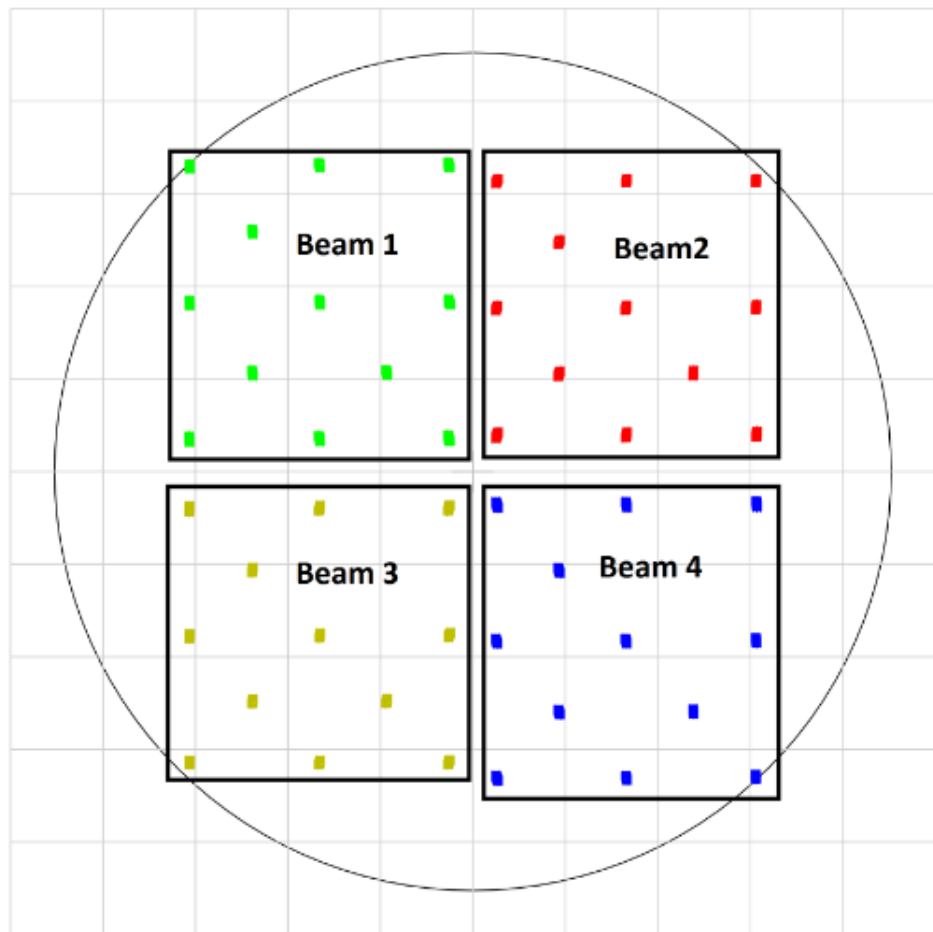


Figure 1.6: 4-beams on 4-CCDs

# Chapter 2

## PSF modeling For WALOP Output From Zemax Simulations

### 2.1 Photometry

Astronomy is all about measuring the amount of energy, in the form of electromagnetic radiation from celestial objects. This quantity we will call the flux. The science of measuring the flux we receive from celestial objects is called photometry. Photometry usually refers to measurements of flux over broad wavelength bands of radiation photometry while in spectroscopic photometry is done for small wavelength intervals. Measurement of flux, when coupled with some estimate of the distance to an object, can give us information on the total energy output of the object (its luminosity), the object's temperature, and the object's size and other physical properties. In our context, we shall be more focusing on stellar photometry.

#### 2.1.1 Stellar Photometry

Stellar photometry is a branch of astronomy that deals with the accurate measurement of the flux of stars and their variations over time. A measuring instrument is more often coupled with other sub instruments (like polarimeter). In sections ahead, I will enlist some of the techniques and their limitations.

#### 2.1.2 Point Spread Functions

Stars are very far( $> 3 \times 10^{15} Km$ ) with a very small relative size(  $10^6 Km$ ) that subject angular spread of about 60 microarcsecs. That is very much like a point source but due to atmospheric turbulence (called seeing) and other effects, we get a star with effective angular spread to be 1 arcsec. The shape of the blur is technically called Point Spread Functions(PSFs). PSFs are shapes of point source observed at our instruments.

Generally, PSFs are of Gaussian profile (due to the central limit theorem) but for some instrument, it deviates very much from the Gaussian. In our case, we observe large deviations from the Gaussian.

#### 2.1.3 Aperture Photometry

Due to PSFs star does not end abruptly on CCD images. If we want to measure most of the light from a star, we need an optimum aperture size(see figure 2.1). Using a big measurement aperture helps to get practically all of the signal but at the same time contribution from the sky, noise increases causing a decrease of signal to noise ratio(S/N)(see figure 2.2). We can

subtract off the average sky signal, regardless of aperture size, but we cannot subtract off the noise associated with the sky signal, and the bigger the aperture, the larger the sky noise in the aperture. We are also afraid of stray photons(contamination) from other sources than the star. I will discuss a few techniques of aperture photometry here.

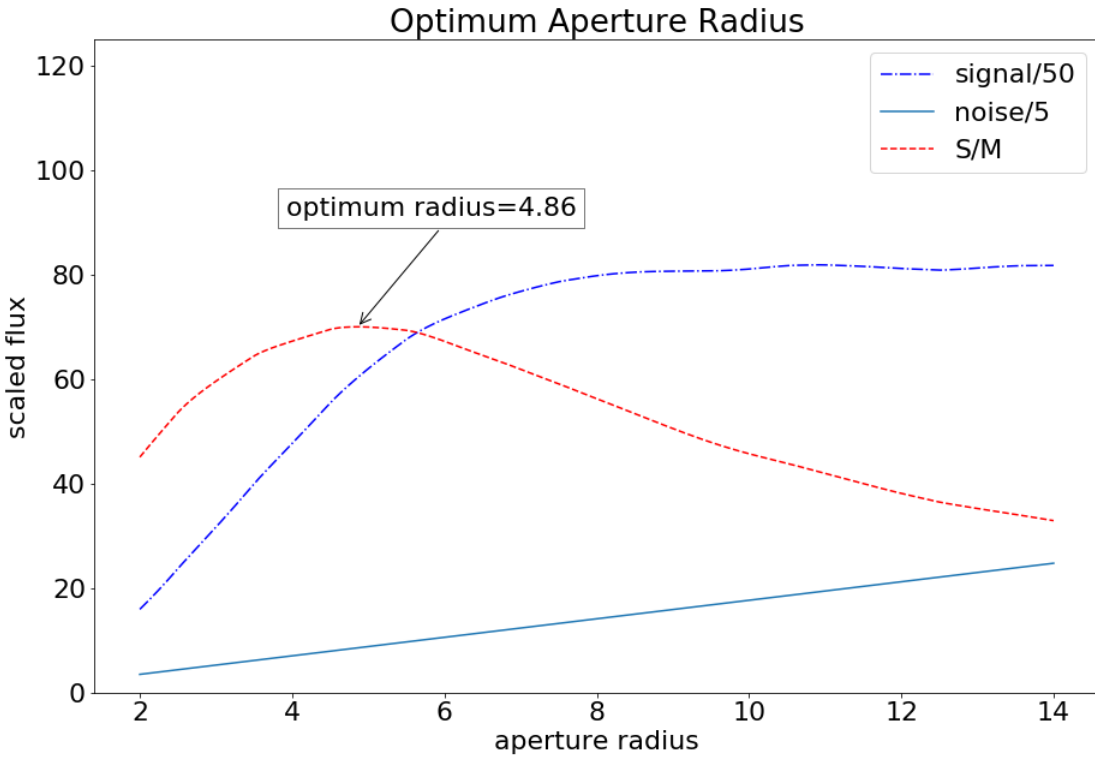


Figure 2.1: Finding an optimum aperture radius for aperture photometry with the growth curve analysis.

We can use aperture correction to bypass some of the above noise. We do photometry of wings(say 1FWHM to 4 FWHM) of the brighter star and scale it down to the fainter star before adding to core(1 FWHM) flux of fainter star.

$$\Delta = m_I(4 \text{ FWHM}) - m_I(1 \text{ FWHM}) \quad (2.1)$$

Here  $\Delta$  is the aperture correction calculated from some bright star. $m_I(4 \text{ FWHM})$  and  $m_I(1 \text{ FWHM})$  are instrumental magnitude of aperture radius of 4 FWHM and 1 FWHM respectively.

Now, when we do photometry of a faint star

$$\text{Flux Total} = m_I(1 \text{ FWHM}) + \Delta \quad (2.2)$$

There are few limitations of aperture photometry,

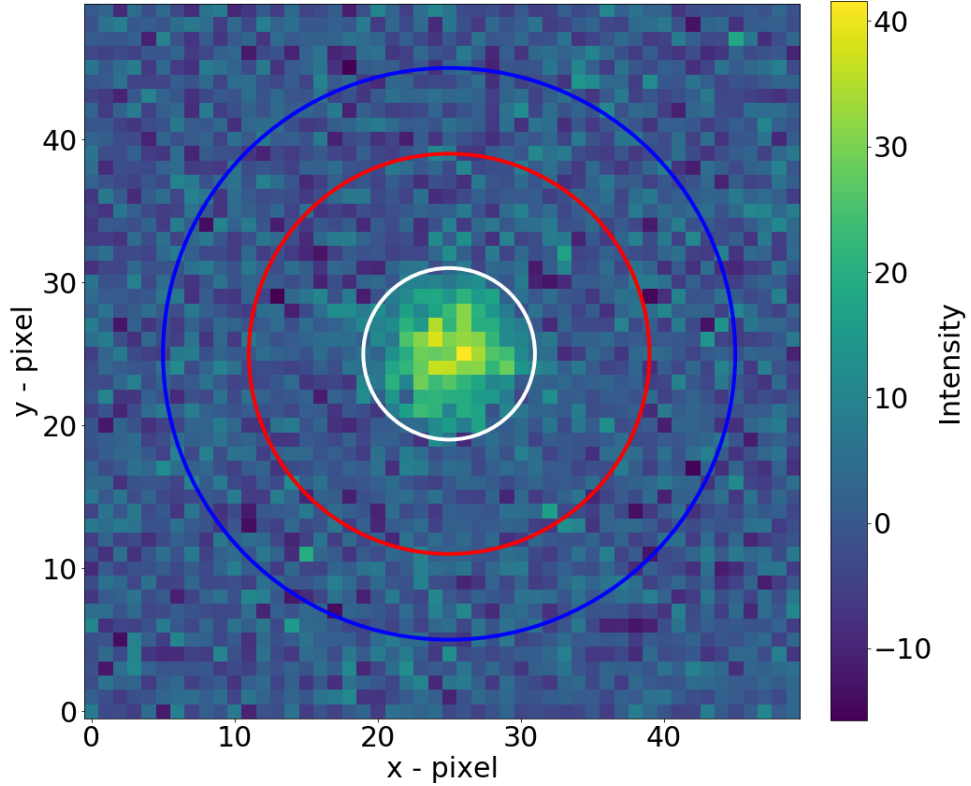


Figure 2.2: Aperture photometry of a background subtracted star. Signal by noise ratio decreases with increase of aperture radius.

For white aperture Radius=6 pixel, Signal flux=1854.74, Noise=53.17 ,and S/N=34.88.

For Red aperture Radius=14 pixel, Signal flux=2090.32, Noise=124.07 ,and S/N=16.84.

For Blue aperture Radius=14 pixel, Signal flux = 2195.85 Noise= 159.52 and S/N = 13.76.

- PSFs are not always of circular symmetry, sometimes we need to use ellipses, so we need to do optimization(see figure 2.1) for other parameters too.
- There is an intrinsic minimum of the noise that we can achieve from the aperture photometry. See figure 2.1, there is a maximum value of S/N, that limits our performance. Even after aperture correction then we are limited by maximum S/N of the brightest star on CCD.
- Sometime PSFs vary with CCD coordinates, so aperture correction could be erroneous.
- Aperture photometry has an assumption of linearly-varying background in the aperture's vicinity. Which is most of the time not true due to contamination(see figure 2.3).
- Aperture photometry fails badly in a crowded field and overlapped stars(see figure 2.4).

### 2.1.4 PSF Photometry

Now we go toward a method that assigns a lower weight to lower S/N pixels and a higher to the higher S/N pixels. For PSF photometry we need to model PSFs (see figure 2.5) with CCD coordinates very accurately. For example PSF photometry with Gaussian PSF of star in figure 2.2 gives, signal  $flux = 2063.095$ ,  $noise = 38.24$ , and  $S/N = 54.29$ . This is quite an improvement from aperture photometry.

$$Flux\ Total = \frac{\sum_i P_i \times PSF_i / \sigma_i^2}{\sum_i PSF_i^2 / \sigma_i^2} \quad (2.3)$$

Here  $P_i$  is the value in  $i^{th}$  pixel and  $PSF_i$  value of PSF in  $i^{th}$  pixel and  $\sigma_i$  sky noise in  $i^{th}$  pixel.

$$\sigma_{total} = \frac{\sigma_{sky}}{\sqrt{\sum_i PSF_i}} \quad (2.4)$$

Here  $\sigma_{total}$  is the total error in a pixel and  $\sigma_{sky}$  is constant sky noise.

PSF photometry is very useful in the following aspects,

- PSFs are generally easy to model and give a really good signal to noise ratio. This benefits in photometry of fainter star.
- Performs well in the crowded field by using iterative subtraction techniques.
- PSF modeling takes care of CCD coordinate variation

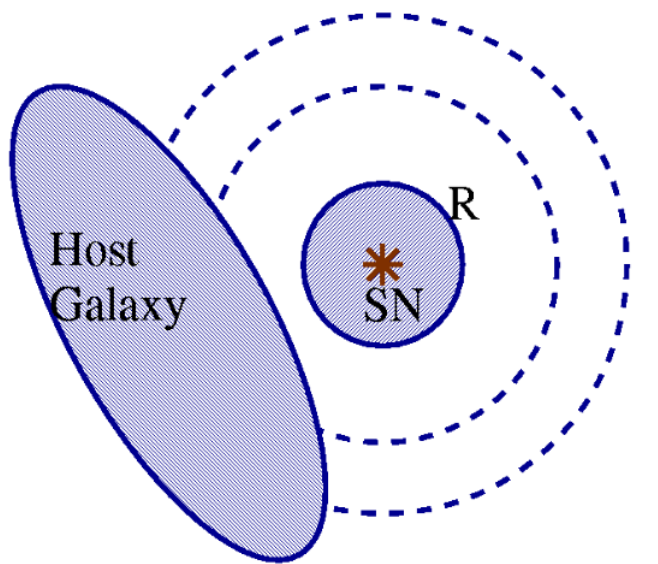


Figure 2.3: Getting contamination from the nearby galaxy while doing aperture photometry of a star(SN).

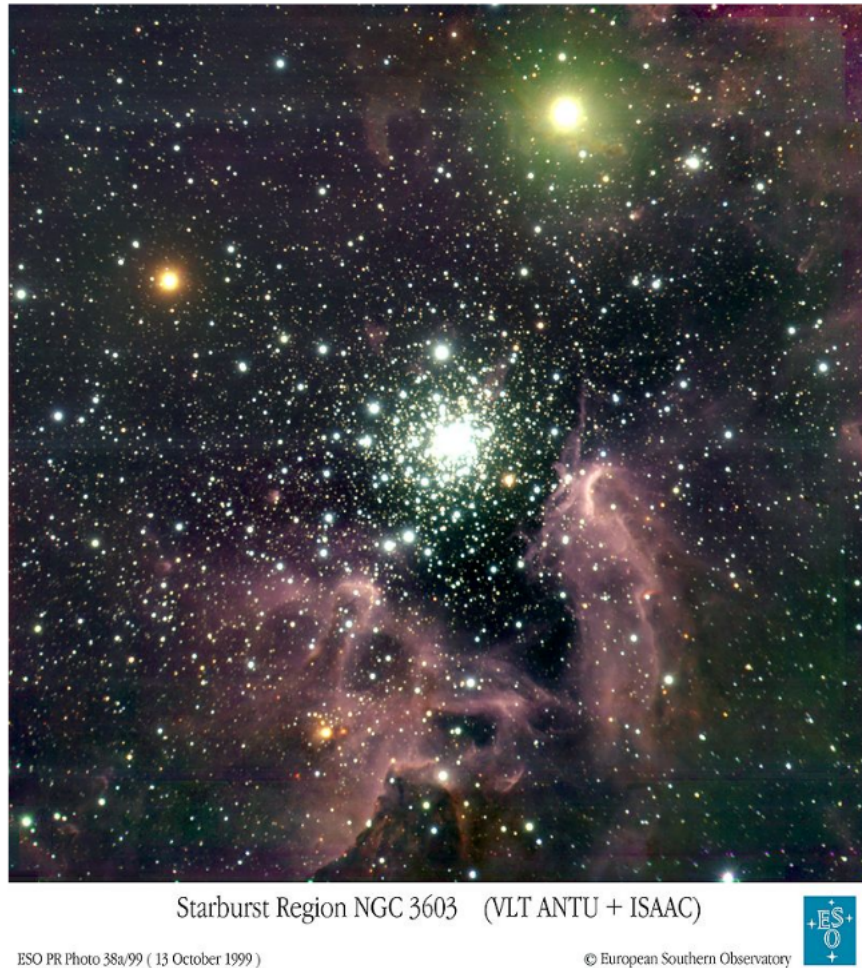


Figure 2.4: Crowded field. Brighter star shadow fainter star giving a tough time for aperture photometry. Overlapped stars can not be handled with aperture photometry.

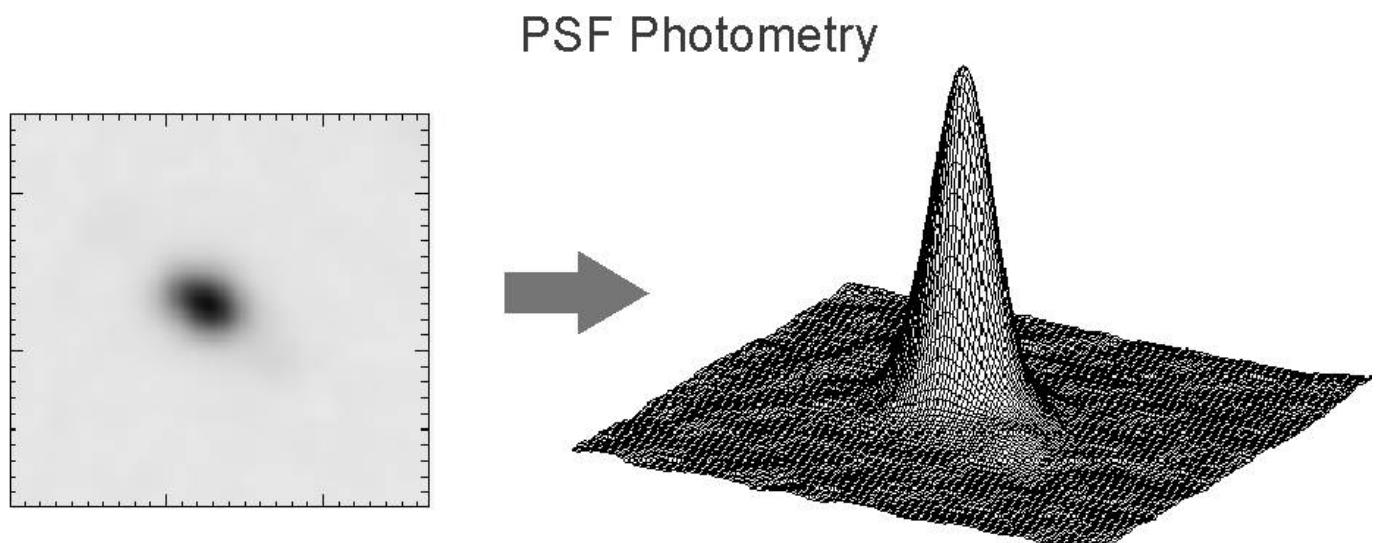


Figure 2.5: A typical PSF.

## 2.2 PSF Modeling For WALOP

Wide Area Linear Optical Polarimeter (WALOP) will cover a field of view of  $30 \times 30$  arcminutes. In ZEMAX simulations we expected PSFs varying with a field of view(see figure 2.6). We need to model these PSFs with CCD coordinates to reach an accuracy of 0.07% in photon counts. We shall explore various possible methods in this section with their limitations. We shall try various available modules and software, some analytical models, and at last some digital models.

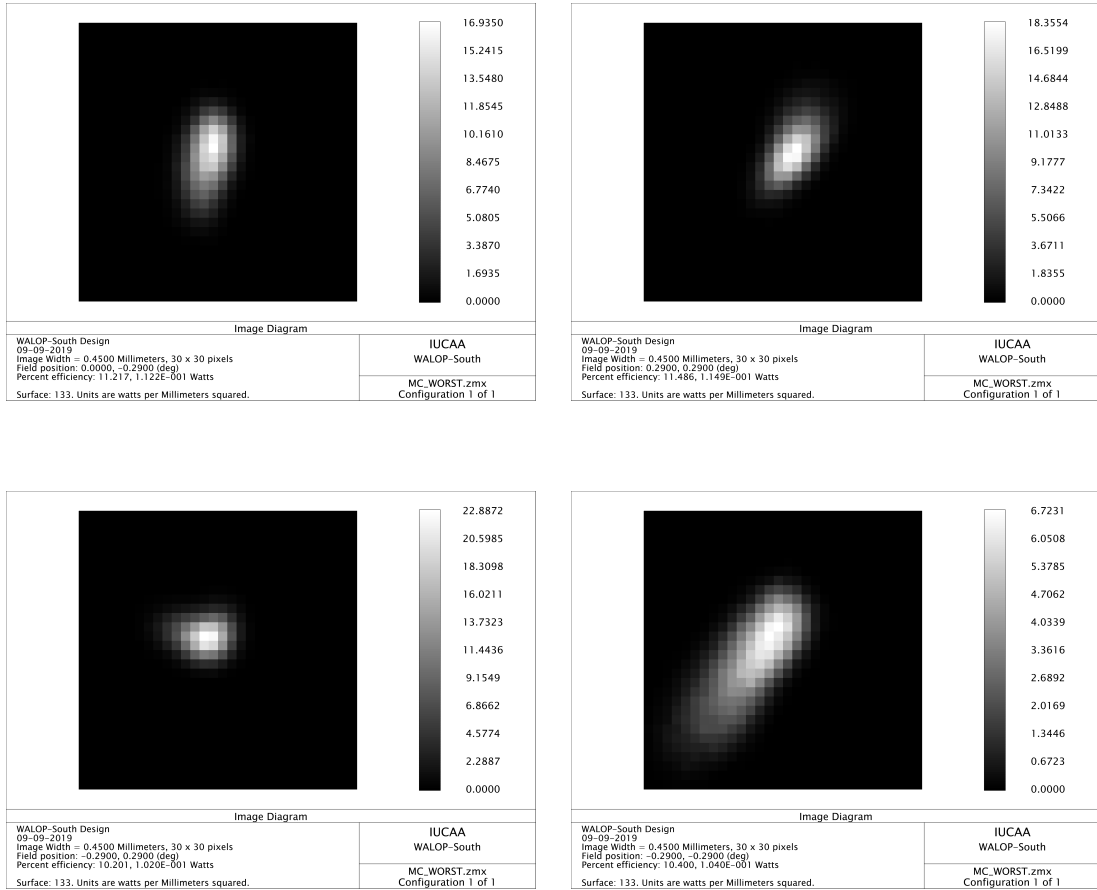


Figure 2.6: Some WALOP PSFs at a different field of view (for worst-case).

### 2.2.1 Available Module and Error Analysis

I tried a python module named Photutils which uses the DAOPHOT algorithm to do photometry in a crowded field. It has almost all useful methods from DAOPHOT and IRAF to perform photometry, star finding, source detection, background estimations, and other tasks.

#### PSF Photometry

Photutils provides a modular set of tools to perform PSF photometry for different science cases. These are implemented as separate classes to do sub-tasks of PSF photometry. It also provides high-level classes that connect these pieces. In particular, it contains an imple-

mentation of the DAOPHOT algorithm proposed by [Stetson](#) in his paper for crowded-field stellar photometry.

The DAOPHOT algorithm consists in applying the loop FIND, GROUP, NSTAR, SUBTRACT, FIND until no more stars are detected or a given number of iterations is reached. DAOPhotPSFPhotometry works as follows. The first step is to estimate the sky background. For this task, photutils provides several classes to compute scalar and 2D backgrounds. The next step is to find an initial estimate of the positions of potential sources. This can be accomplished by using source detection algorithms.

After finding sources one would apply a clustering algorithm to label the sources according to groups. Usually, those groups are formed by a distance criterion, which is the case of the grouping algorithm proposed by Stetson. The reason behind the construction of groups is illustrated as follows: imagine that one would like to fit 300 stars and the model for each star has three parameters to be fitted. If one constructs a single model to fit the 300 stars simultaneously, then the optimization algorithm will have to search for the solution in a 900-dimensional space, which is computationally expensive and error-prone. Reducing the stars in groups effectively reduces the dimension of the parameter space, which facilitates the optimization process.

Provided that the groups are available, the next step is to fit the sources simultaneously for each group. This task can be done using an astropy fitter, for instance, LevMarLSQFitter.

After sources are fitted, they are subtracted from the given image and, after fitting all sources, the residual image is analyzed by the finding routine again to check if there exists any source which has not been detected previously. This process goes on until no more sources are identified by the finding routine.

### **Building a PSF model From CCD Image**

The instrumental PSF is a combination of many factors that are generally difficult to model. [Anderson and King \(2000; PASP 112, 1360\)](#) showed that accurate stellar photometry and astrometry can be derived by modeling the net PSF, which they call the effective PSF (ePSF). The ePSF is an empirical model describing what fraction of a star's light will land in a particular pixel.

It takes good stars cutouts (see figure 2.7) to fit various free parameters from the model. Ideally, these stars should be bright (high S/N) and isolated to prevent contamination from nearby stars. The process involves iterating between the ePSF itself and the stars used to build it. This PSF model is then used in PSF photometry.

### **Best Case of Zemax Output**

We used the above method(sec:2.2.1) to perform photometry for the best case output from the ZEMAX simulation of WALOP. The best case has all the distortion effect adding up to give an effective Gaussian distortion(Central limit theorem). We got maximum error of 0.6% and a median of 0.3%(see figure 2.8). But this is way far less than our requirement. We want to measure polarization up to 0.1% that is why the error of 0.3% is hazardous.

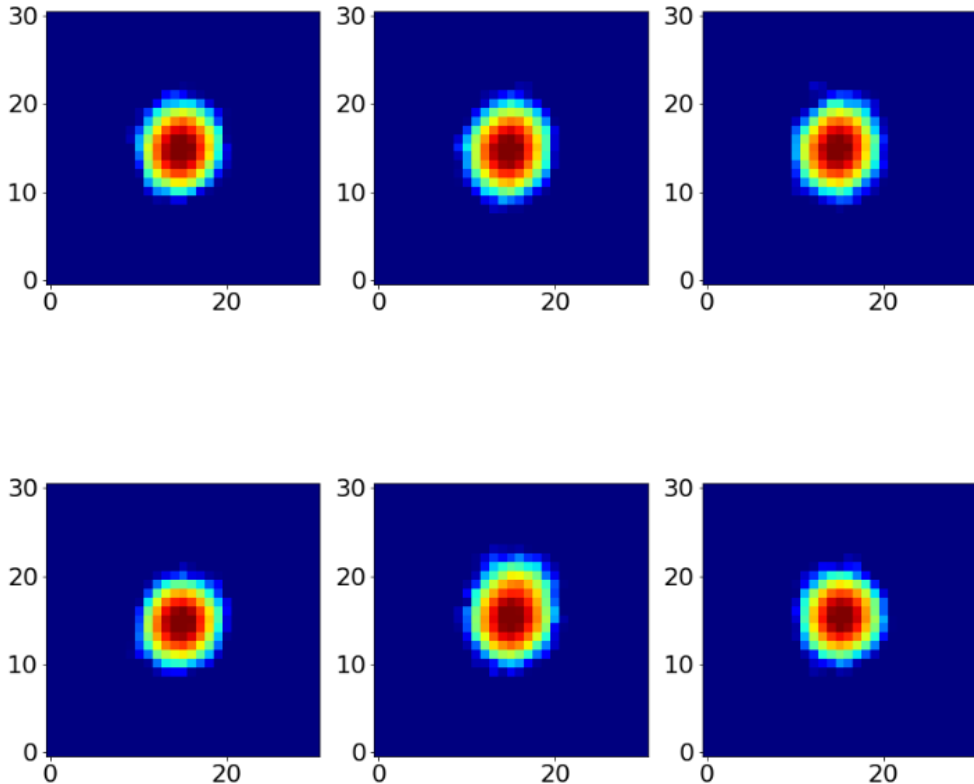


Figure 2.7: Some good star cutouts in  $30 \times 30$  pixels from the best case ZEMAX output.

### Worst Case of Zemax Output

In the worst-case output, all distortion effects add up in one direction to give a worse distortion. We analyzed the worst output from the above module and got a maximum of 10% error with a median 1.2% error(see figure 2.9). This is a huge setback.

We need a far better PSF model to achieve the desired accuracy. We plan to customize our model into the Photutils module, we will pull GitHub projects if needed. Before that, we explore some possibilities with other analytical models.

#### 2.2.2 Analytical Model

In this section, we will try to model some examples of the worst case of ZEMAX output with some analytical model. We tried some of the orthogonal 2D polynomials to fit the PSF.

##### Zernike Polynomials

Zernike Polynomials are a sequence of polynomials that are orthogonal on the unit disk(see figure 2.10). There are even and odd Zernike polynomials. The even ones are defined as,

$$Z_n^m(\rho, \varphi) = R_n^m(\rho) \cos(m\varphi)$$

and the odd ones as,

$$Z_n^{-m}(\rho, \varphi) = R_n^m(\rho) \sin(m\varphi),$$

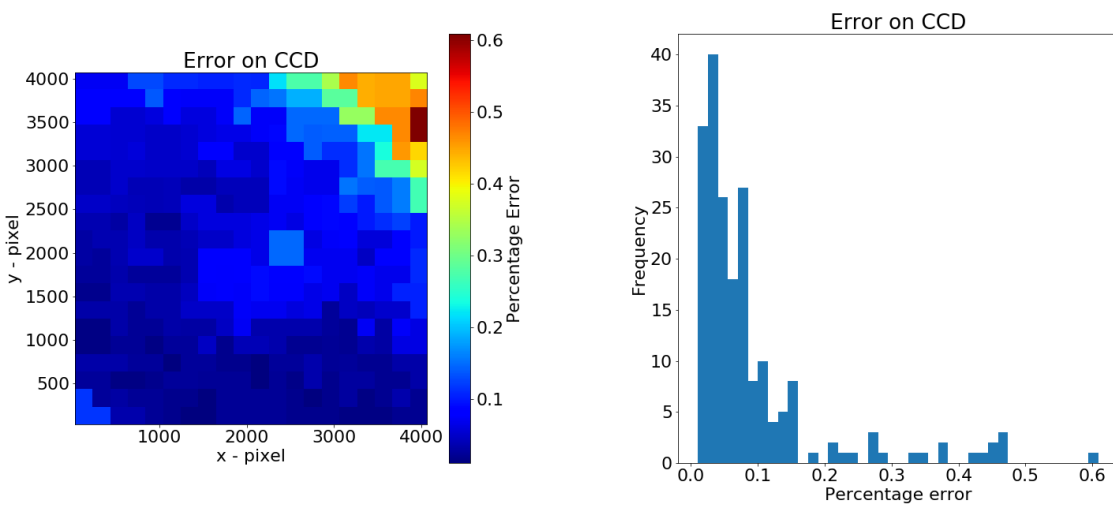


Figure 2.8: Error analysis of the PSF photometry by Photutils with the best case of Zemax output.

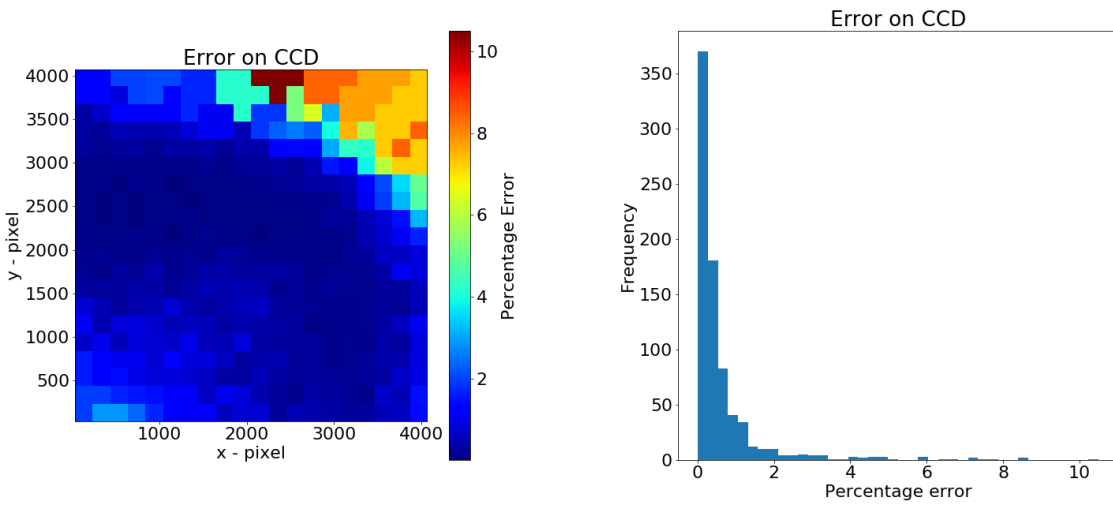


Figure 2.9: Error analysis of the PSF photometry by Photutils with the worst case of Zemax output.

where  $m$  and  $n$  are non-negative integers with  $n \geq m$ ,  $\varphi$  is the azimuthal angle,  $\rho$  is the radial distance  $0 \leq \rho \leq 1$  and  $R_n^m$  are the radial polynomials defined below. Zernike polynomials have the property of being  $|Z_n^m(\rho, \varphi)| \leq 1$ . The radial polynomials  $R_n^m$  are defined as,

$$R_n^m(\rho) = \sum_{k=0}^{\frac{n-m}{2}} \frac{(-1)^k (n-k)!}{k! (\frac{n+m}{2}-k)! (\frac{n-m}{2}-k)!} \rho^{n-2k}$$

We have PSFs not limited to unit disk and also they vanish at infinity. We made some changes,

$$\rho = 1 - \exp\left(\frac{-r}{\lambda}\right)$$

The above transformation removes the limitation of unit disk and where  $\lambda$  is the parameters of the size of the PSF. We tried fitting following hybrid function(due to [L. W. Piotrowski et al. 2013](#)),

$$PSF(r, \varphi) = \exp\left(-r^p \sum_{n,m} b_{n,m} Z_n^m(\rho, \varphi)\right),$$

where  $p$  is characterizing asymptotic behavior of PSF,  $b_{n,m}$  are fitting parameters. Some feasible PSFs are made from the help of Zernike polynomials(see figure [2.11](#), [2.12](#)). This suggests that they can be useful in fitting real PSFs.

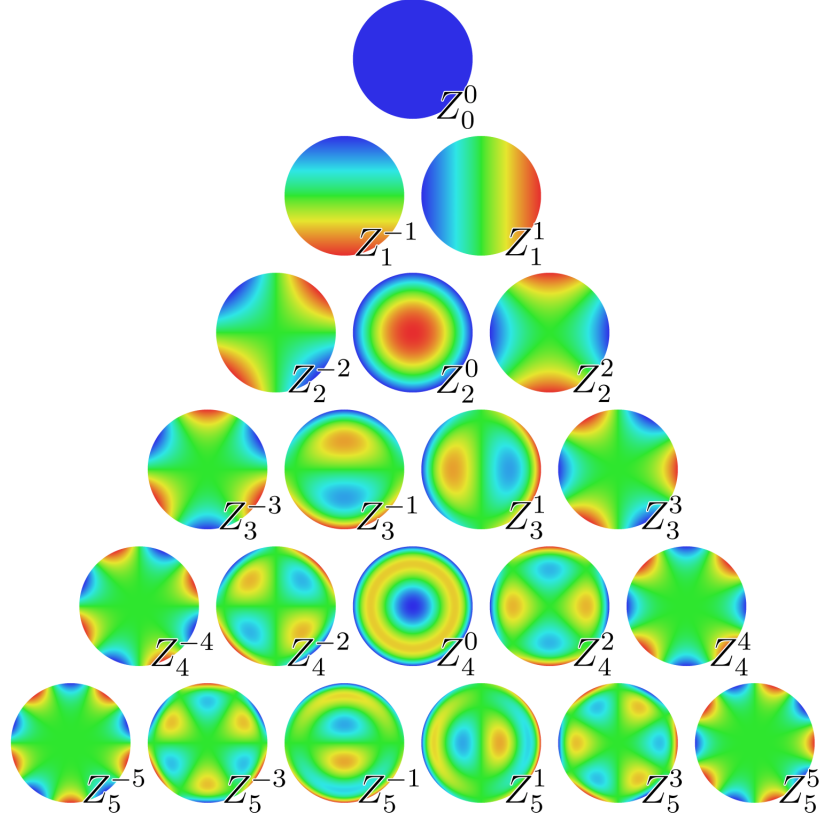


Figure 2.10: The first 21 Zernike polynomials( $Z_n^m$ ) in unit disk. Where  $n$  is the radial degree and  $m$  is the azimuthal degree.

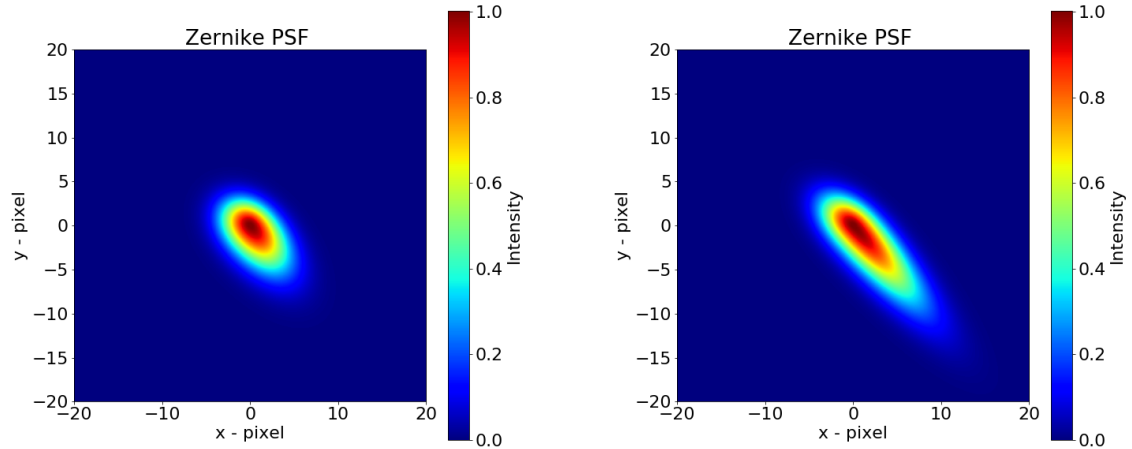


Figure 2.11: Some typical PSFs made from Zernike Polynomials. Left:  $p = 2.0$ ,  $b_{2,0} = 0.1$ ,  $b_{1,-1} = 0.04$ , and  $b_{2,-2} = 0.04$ . Right:  $p = 2.0$ ,  $b_{2,0} = 0.1$ ,  $b_{1,-1} = 0.036$ , and  $b_{2,-2} = 0.065$ .

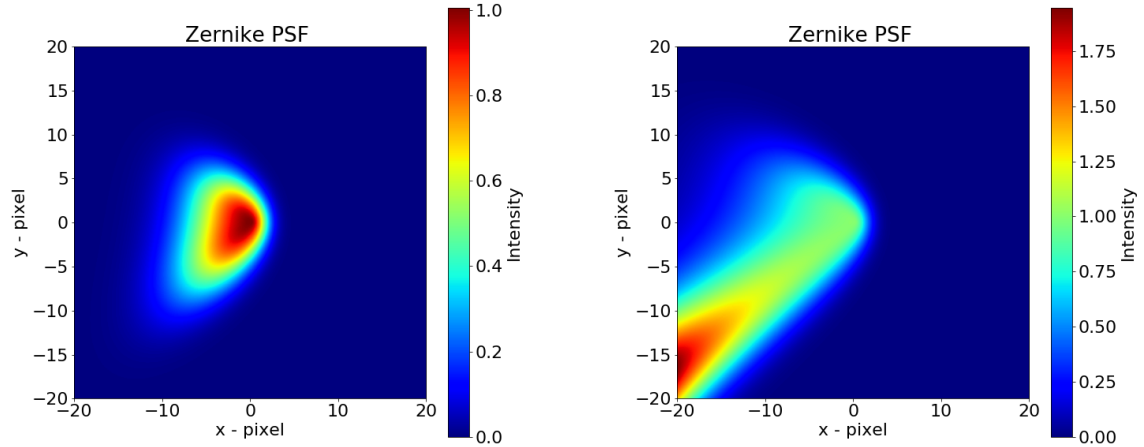


Figure 2.12: Left:  $p = 2.0$ ,  $b_{2,0} = 0.1$ ,  $b_{1,-1} = 0.007$ ,  $b_{1,1} = 0.12$  and  $b_{4,2} = 0.04$ . Right:  $p = 2.0$ ,  $b_{2,0} = 0.1$ ,  $b_{1,-1} = 0.007$ ,  $b_{1,1} = 0.13$  and  $b_{4,2} = 0.04$ . See how unstable the PSF is with respect to the parameter  $b_{1,1}$ .

There are few limitations of Zernike polynomials model,

- Zernike Polynomials are orthogonal in the unit disk, but we are trying to fit an exponential of Zernike which is not orthogonal to each other. Many combinations of parameters can give the same result.
- This is probably very much sensitive to parameters(due to exponential), making fitting very difficult(see figure 2.12)
- This is a very complicated function and also a transformation involved not worth working because digital models or other analytical models can give better results with less complicity.
- In the parent paper it is reported to reach 13 % accuracy but that is not enough for us. But it was my first work in this direction so it worth trying.

### Polar Shapelets

Polar shapelets are another analytical 2D polynomials with desired properties. The shapelet method for image analysis is based upon the decomposition of localized objects into a series of orthogonal components with convenient mathematical properties. Unlike Zernike Polynomials these are proved to be orthogonal and complete in all space.

The polar shapelet basis functions  $\chi_{n,m}(r, \varphi; \beta)$  are also parameterized by two integers,  $n$  and  $m$ , and a smooth function  $f(r, \varphi)$  in polar coordinates may be decomposed into polar shapelets as following.

$$f(r, \varphi) = \sum_{n=0}^{n=\infty} \sum_{m=-n}^{m=n} b_{n,m} \chi_{n,m}(r, \varphi; \beta),$$

where  $b_{n,m}$  are shapelets coefficients and  $\beta$  is Gaussian scale factor, which we need to fit. $n$  is any positive integer and  $m$  is between  $-n$  to  $n$  in step to two.

The polar shapelet coefficients  $b_{n,m}$  are again given by the “overlap integral”

$$b_{n,m} = \int \int_R f(r, \varphi) \chi_{n,m}(r, \varphi; \beta) dr d\varphi$$

Few points for polar shapelets,

- This is not limited to unit disk and can be used directly as image components, unlike Zernike Polynomials.
- These are very intuitive in nature and widely used for morphological classification of images. Detailed analysis is in next chapter.

### Elliptical Gaussian

Elliptical Gaussian is a classical function used for modeling very simple PSFs (due to Paul L. Schechter et al. 1993). These are simple functions with only three parameters for modeling, making it easy and practical to fit.

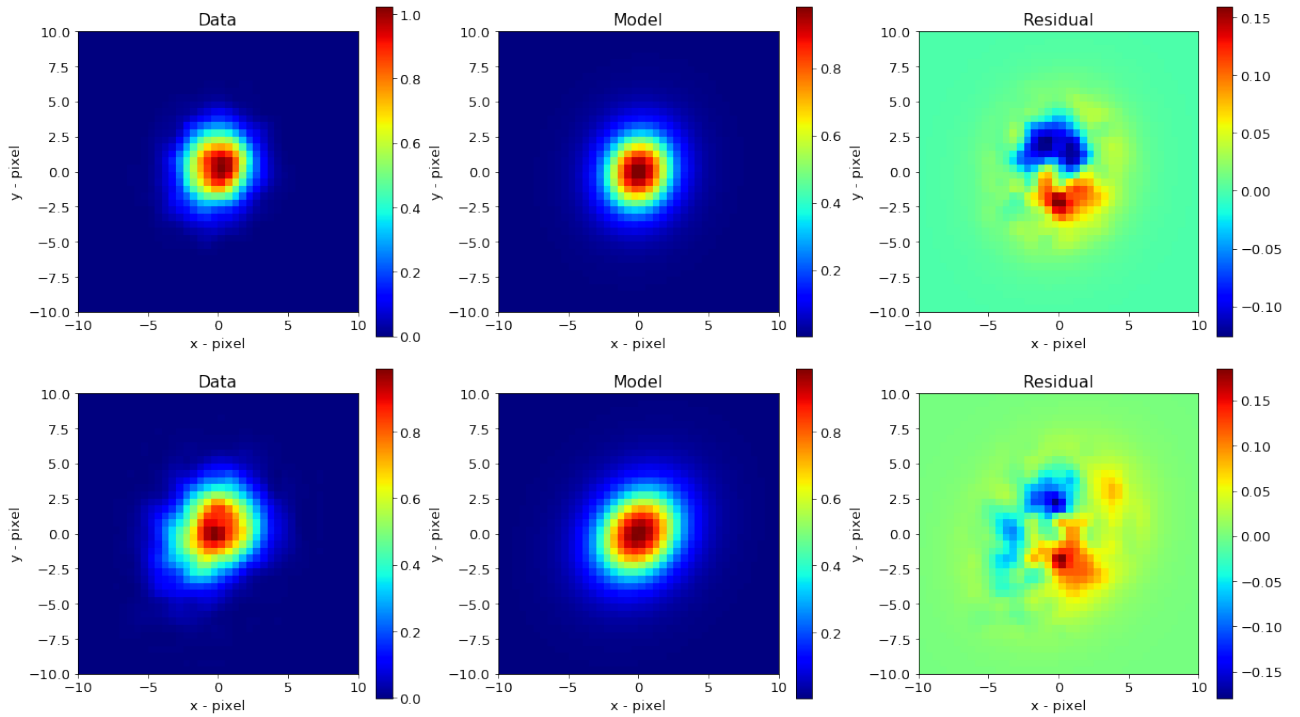


Figure 2.13: Some random star cutouts fitted with elliptical Gaussian. Top:  $\sigma_x = 3.620$ ,  $\sigma_y = 4.598$  and  $\sigma_{xy} = -0.038$  with  $I_o = 1.0$ . Bottom :  $\sigma_x = 3.315$ ,  $\sigma_y = 4.167$  and  $\sigma_{xy} = -0.023$ .

$$I(x, y) = I_o \left( 1 + z^2 + \frac{1}{2} \beta_4 z^4 + \frac{1}{6} \beta_6 z^6 \right),$$

where,

$$z^2 = \frac{1}{2} \left( \frac{x^2}{\sigma_x^2} + 2\sigma_{xy}xy + \frac{y^2}{\sigma_y^2} \right),$$

here  $\sigma_x$ ,  $\sigma_y$  and  $\sigma_{xy}$  are free parameters to fit with data.  $\beta_4$  and  $\beta_6$  are perturbation parameter adjusted to give good residuals.  $I_o$  is scaling parameter which vary with stars.

We see figures 2.13, some of the residuals have some pattern so we have to model residuals by other means. Benefits of modeling with elliptical Gaussian,

- Unlike Zernike Polynomials and Polar shapelets, No coordinate transformation(Cartesian to cylindrical) is required.
- Most of the region (around the center) of CCD can be modeled alone with this. For the corner part, we will have to model residuals too.

# Chapter 3

## PSF modeling For WALOP Output Using Polar Shapelets

### 3.1 Polar Shapelets

The shapelet method for image analysis is based upon the decomposition of localized objects into a series of orthogonal components with convenient mathematical properties. Polar shapelets are polynomial function of polar coordinates( $r, \varphi$ ). They are orthogonal and complete basis functions in complex space. Unlike Zernike Polynomials these are proved to be orthogonal and complete in all space. In principle, any image can be dissociated into polar shapelets.

The polar shapelet basis functions  $\chi_{n,m}(r, \varphi; \beta)$  are also parameterized by two integers,  $n$  and  $m$ , and a smooth function  $f(r, \varphi)$  in polar coordinates may be decomposed into polar shapelets. We aim to decompose our PSF into polar shapelets as following

$$PSF(r, \varphi) = \sum_{n=0}^{n=\infty} \sum_{m=-n}^{m=n} b_{n,m} \chi_{n,m}(r, \varphi; \beta), \quad (3.1)$$

where  $b_{n,m}$  are shapelets coefficients and  $\beta$  is the Gaussian scale factor.  $n$  is any positive integer and  $m$  is integers between  $-n$  to  $n$  in step to two.

Polar shapelets hold following orthogonal and complete properties.

$$\int \int_R \chi_{n,m}^*(r, \varphi; \beta) \chi_{u,v}(r, \varphi; \beta) r dr d\varphi = \delta_{n,m} \delta_{u,v},$$

here  $\delta$  is the Kronecker delta and the asterisk denotes complex conjugation.

$$\sum_{n=0}^{n=\infty} \sum_{m=-n}^{m=n} \chi_{n,m}(r, \varphi; \beta) \chi_{n,m}(r', \varphi'; \beta) = \delta(r - r') \delta(\varphi - \varphi').$$

here  $\delta$  is the Dirac delta.

By multiplying both sides of the equation 3.1 by  $\chi_{n,m}(r, \varphi; \beta)$ , integrating over all space and using orthogonal property, we get the “overlap integral” as

$$b_{n,m} = \int \int_R PSF(r, \varphi) \chi_{n,m}(r, \varphi; \beta) r dr d\varphi. \quad (3.2)$$

Above are some general structure of polar shapelets which are very helpful in our analysis

but the analytical definition of polar shapelets are followings,

$$\chi_{n,m}(r, \varphi; \beta) = \frac{(-1)^{\frac{n-|m|}{2}}}{\beta^{|m|+1}} \left[ \frac{\left(\frac{n-|m|}{2}\right)!}{\pi \left(\frac{n+|m|}{2}\right)!} \right]^{\frac{1}{2}} \times r^{|m|} L_{\frac{n-|m|}{2}}^{|m|} \left( \frac{r^2}{\beta^2} \right) \exp \left( \frac{-r^2}{2\beta^2} \right) \exp(im\varphi).$$

The associated Laguerre polynomials( $L_n^k$ ) are given explicitly by the formula

$$L_n^k(x) = \frac{1}{n!} \sum_{i=0}^{i=n} \frac{n!}{i!} ({}^{k+n}C_{n-i})(-x)^i.$$

Few polar shapelets(real part) are plotted in figure 3.1. We can use these polar shapelets to model our PSFs.

### 3.2 Star Specifications

Real stars are approximately Gaussian PSF on the focal plane of the telescope. Mounted sub-instruments introduces further distortion to the Gaussian PSF, making it irregular. To model these distortions, we also used Gaussian PSF as the input of the Zemax simulation of WALOP. We prepared a  $100 \times 100$  pixels image imitating Gaussian PSF. The numbers of photons we receive from the source also depends on the specification of the telescope we are using. Following are the telescope settings(to closely resemble real stars) at South African Astronomical Observatory(SAAO).

- $D_o = 100.0\text{cm}$ , outer diameter of the telescope.
- $D_i = 25.00\text{cm}$ , inner diameter of the telescope.
- $A = \frac{1}{4}\pi(D_0^2 - D_i^2)$ , effective area of the telescope.
- $B = 5000\text{ A}^\circ$ , bandwidth of the guider camera band.  $1000\text{ A}^\circ$  is the approximate bandwidth of the V band filter.
- We do not receive all photons from the sky patch, most of them are absorbed by telescope and guider systems. From the telescope manual we have efficiency of the telescope plus the guider system to be  $e = 0.3$ .
- $p = 0.5\text{ arcsec}$ , pixel size of the CCD in arcseconds. This measures the area of the sky patch covered by CCD.
- $f_v = 1000\text{ photons cm}^{-2} t^{-1} A^\circ{}^{-1}$ ,  $f_v$  is flux of 0 magnitude, V band star. We compare this flux value to get relative flux of other stars in the same band.

The total flux of the star and sky background in the V band can be calculated for given magnitudes(star and background) by the following formula.

$$N = f_v A B t e 10^{\frac{m_{star}}{2.512}}, \quad (3.3)$$

here  $N$  is the total photons received form the star of the magnitude  $m_{star}$ . Sky background can be estimated by,

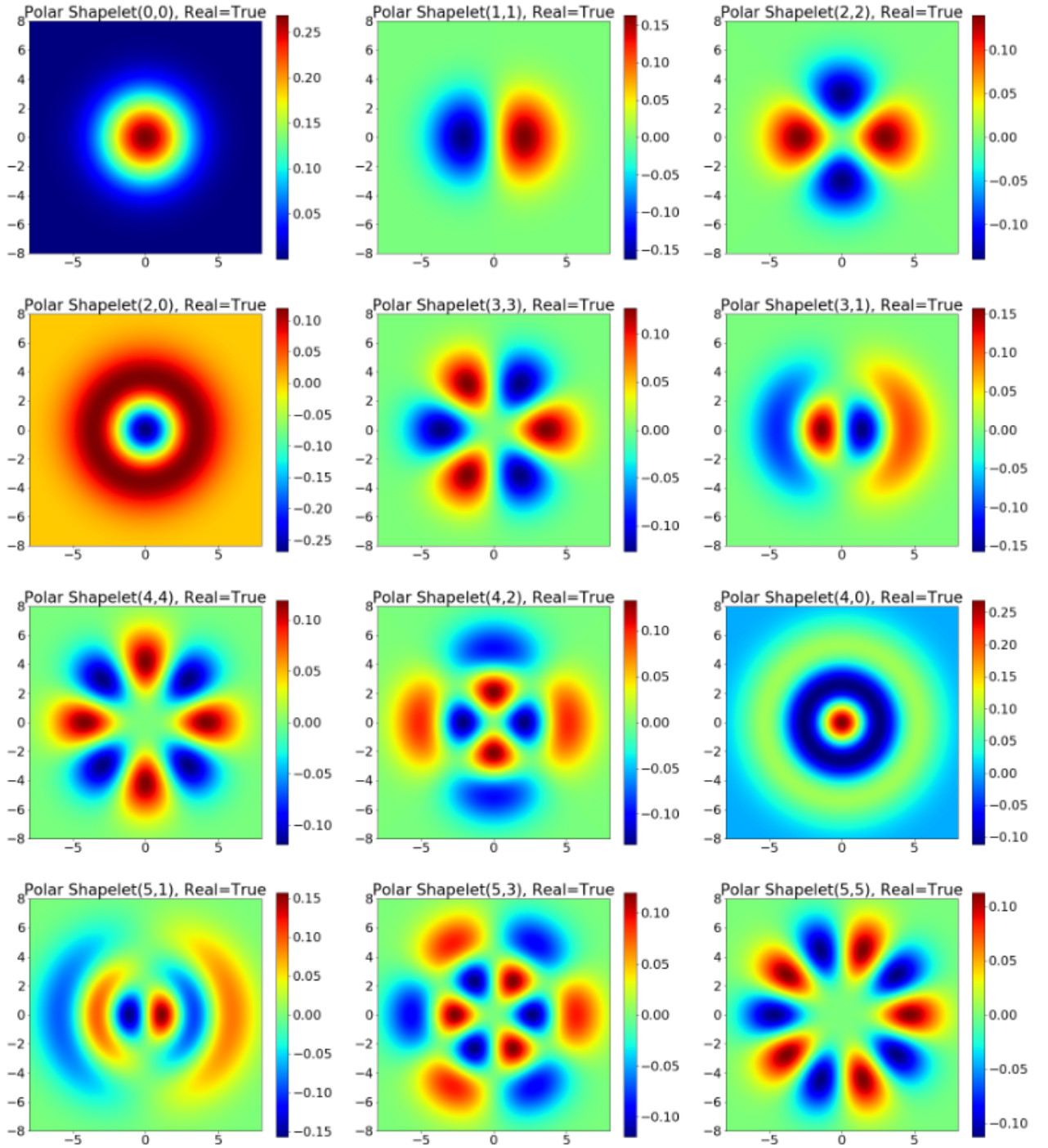


Figure 3.1: The real part of the polar shapelets (for  $\beta = 2.1$ ) and different combinations of  $n$  and  $m$  values. Each image is plotted for x and y axis form  $-8$  to  $8$ , colorbar represents the numerical value of the polar shapelet.

$$n_{sky} = \frac{N}{p^2 (m_{sky} - m_{star})},$$

here  $n_{sky}$  is sky background, photon per arcsec square per unit time.

We created a Gaussian( $\sigma = 4$ ) pixels star on a  $100 \times 100$  pixels image with above specifications.

### 3.3 Zemax Input Images

1000 random points were drawn on an input image of  $4096 \times 4096$  pixels and saved as stars coordinates. Points were kept at a minimum distance of 80 pixels so that they don't overlap with each other. At each point, a Gaussian star was imposed. Now we have a typical sky view( $4096 \times 4096$ ) with 1000 stars on it(see figure 3.2).

Three class of images were created for analysis purposes. The fist was 1000 stars with Poisson noise at random positions of  $4096 \times 4096$  pixels CCD image, the second was just sky background with magnitude 20 and the third was 1000 stars with sky background respecting Poisson statistics at the same random positions(as the first) of  $4096 \times 4096$  pixels CCD image.

These input images were made to pass through the Zemax simulation of WALOP and outputs were analyzed.

These processes were performed with different magnitudes of stars in input images.

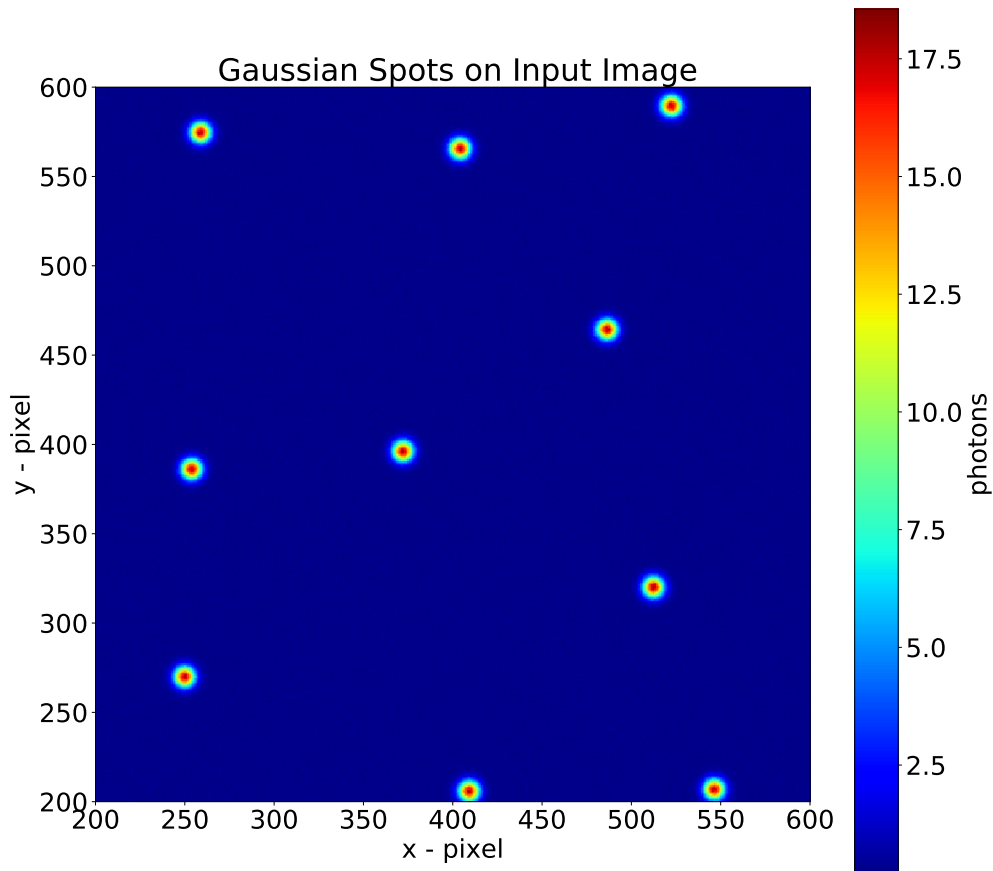


Figure 3.2: A small part of a input image with random stars.

### 3.4 Processing Zemax Output Images

For processing output images we made and saved star cutouts (as in figure 2.7) for all output images (with noise, without noise for various star magnitudes). Clean star cutouts were used to make PSF models and these models were used to perform photometry of noisy star cutouts. We present the PSF modeling process in the next section and photometry error analysis in the next chapter.

### 3.5 Exposure Time Analysis

For the above analysis, we took the time of exposure to  $1\text{ s}$  but we need more exposure time to measure fainter stars. We performed an exercise to get an idea about the suitable exposure time for star magnitude as per our error tolerance.

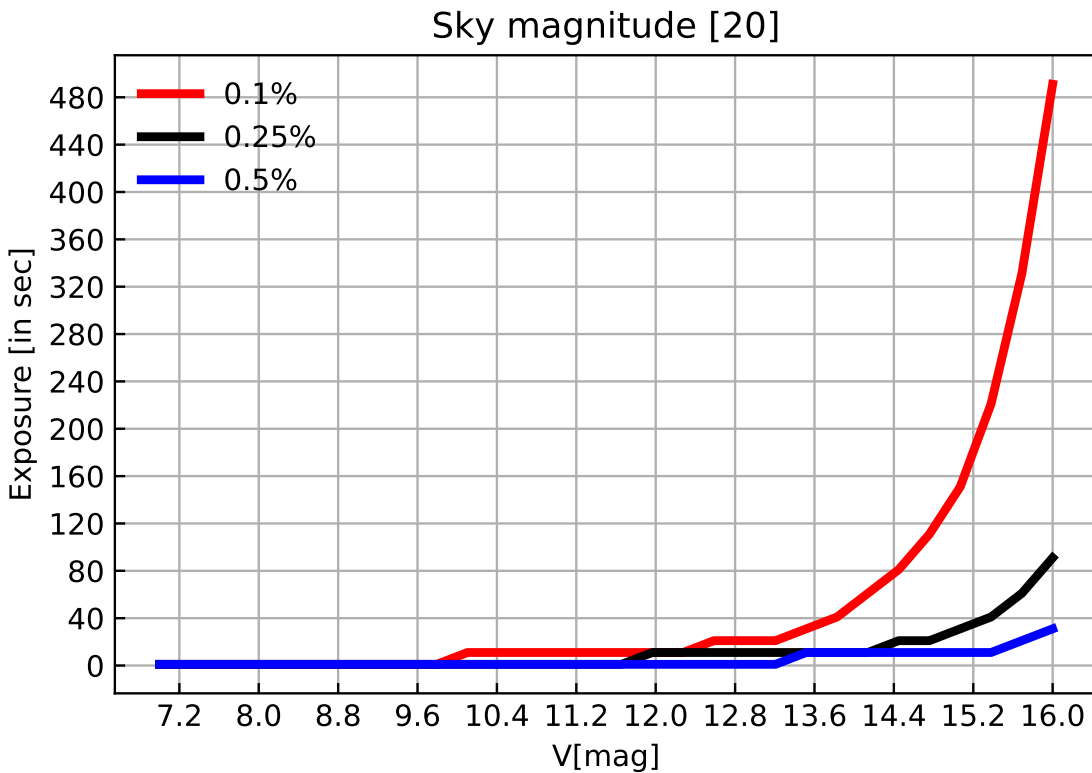


Figure 3.3: Trace of required exposure time to achieve various error tolerance.

We created Gaussian stars with above mentioned specifications for various magnitudes ( $m_{star}$ ) and exposure time( $t$ ). We estimated the exposure time required to reach a given error tolerance and traced a plot (see figure 3.3). We kept the sky background fixed because relative flux( $\Delta m$ ) is all that matters in magnitude system. We observe (in the plot) that to measure a 16 magnitude star in V band with an error of 0.1%, we require an exposure time of 480 s. This analysis will be useful in deciding the optimal exposure time of the telescope for a different patch of sky.

### 3.6 Steps Taken for PSF Modeling

The following steps were taken to model WALOP PSF with polar shapelets.

- We calculated real and imaginary part of all required polar shapelets(upto  $n = 5$ ) for  $x$  and  $y$  from  $-8$  to  $8$ ( $\beta = 2.1$ ), saving them into  $1000 \times 1000$  matrices(see figure 3.1) for future access. This reduces computational time of the code drastically.
- We Interpolated star cutouts(see data images of figure 3.5 from  $100 \times 100$  to  $1000 \times 1000$  matrices(same as polar shapelets) followed by Gaussian smoothing(of sigma 5 pixel) and normalization.
- We rolled each image in such a way that the maximum is at the center of the image.
- Performed simple 2-D Numpy array multiplication of star cutouts( $1000 \times 1000$ ) with the real and imaginary image( $1000 \times 1000$ ) of polar shapelets to get real and imaginary part of  $b_{n,m}$  respectively. This is equivalent to the integration in the equation ??.
- By equating real part of equation 3.1. we get

$$PSF \approx \sum_{n=0}^{n=6} \sum_{m=-n}^{m=n} Re(b_{n,m}) Re(\chi_{n,m}) - Im(b_{n,m}) Im(\chi_{n,m}),$$

here PSF is 2-D matrix as  $\chi_{n,m}$  are. Imaginary parts tends to zero. Above is the model of PSF which recovers most of the pattern of PSF.

We computed volume under the PSF and star image and their difference as a metric of accuracy for our modeling.

### 3.7 Results

We see figures 3.5, none of the residuals have a regular pattern. We used polar shapelets upto  $n = 6$  with a total of 28 parameter. The median of percentage volume error found to be 0.11. In the next chapter, we will use this model to estimate the total flux of stars(noisy image) and error associated.

- We have chosen our error metric to be volume error along with the graphical plots ,  

$$Error\% = \frac{Sum(Data) - Sum(Model)}{Sum(Data)} \times 100.$$
- We have achieved an excellent level of accuracy in analytical modeling. In polar shapelet modeling, we do not need to model the residuals(unlike elliptical Gaussian models in figure 2.13). This can model very complicated features form PSF, in-fact this can model any 2D image(will further explain in Chapter 5).
- Median of percentage volume error found to be 0.11. This is a rough estimation of modeling accuracy, real testing of the model will be on photometry.
- We have been using, 2D Gaussian, Moffat Lorentzian and other functions to model PSF, but most of them were not able to capture elliptical asymmetry(in figure 2.13) but we see that polar shapelets can capture all kinds of asymmetry in PSF.

- So far so good but to perform actual photometry we need to under-sample the PSF to the matrix shape of star cutouts.
- This is very simple to model and no fitting is involved (like curve fit or least square fit). This is also light in computation. For an optimized version of code, the whole process of modeling is just a few matrix multiplications.
- Parameters are smoothly varying with CCD coordinates. We plan to divide CCD into some optimum part to perform further photometry.
- In this technique, we need to find the maxima of the star and roll them into the center. This is not very practical (sudden cosmic ray burst gives irregular maxima) way in real life. We need to find some other central tendency (like centroid) and test our photometry code.

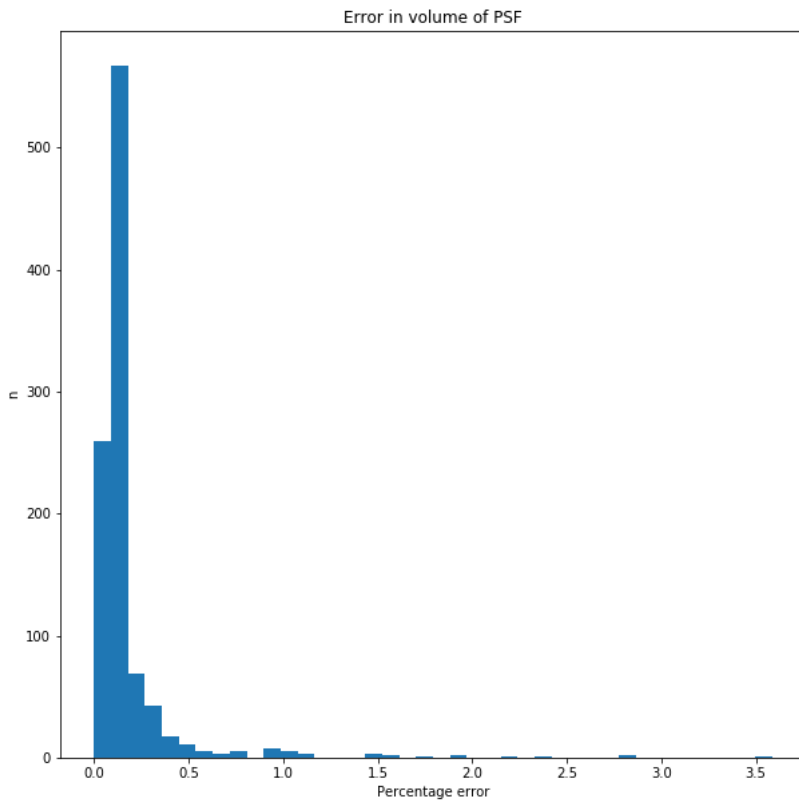


Figure 3.4: Histogram of photometric error in PSF modeling (For 1000 random star points on CCD).

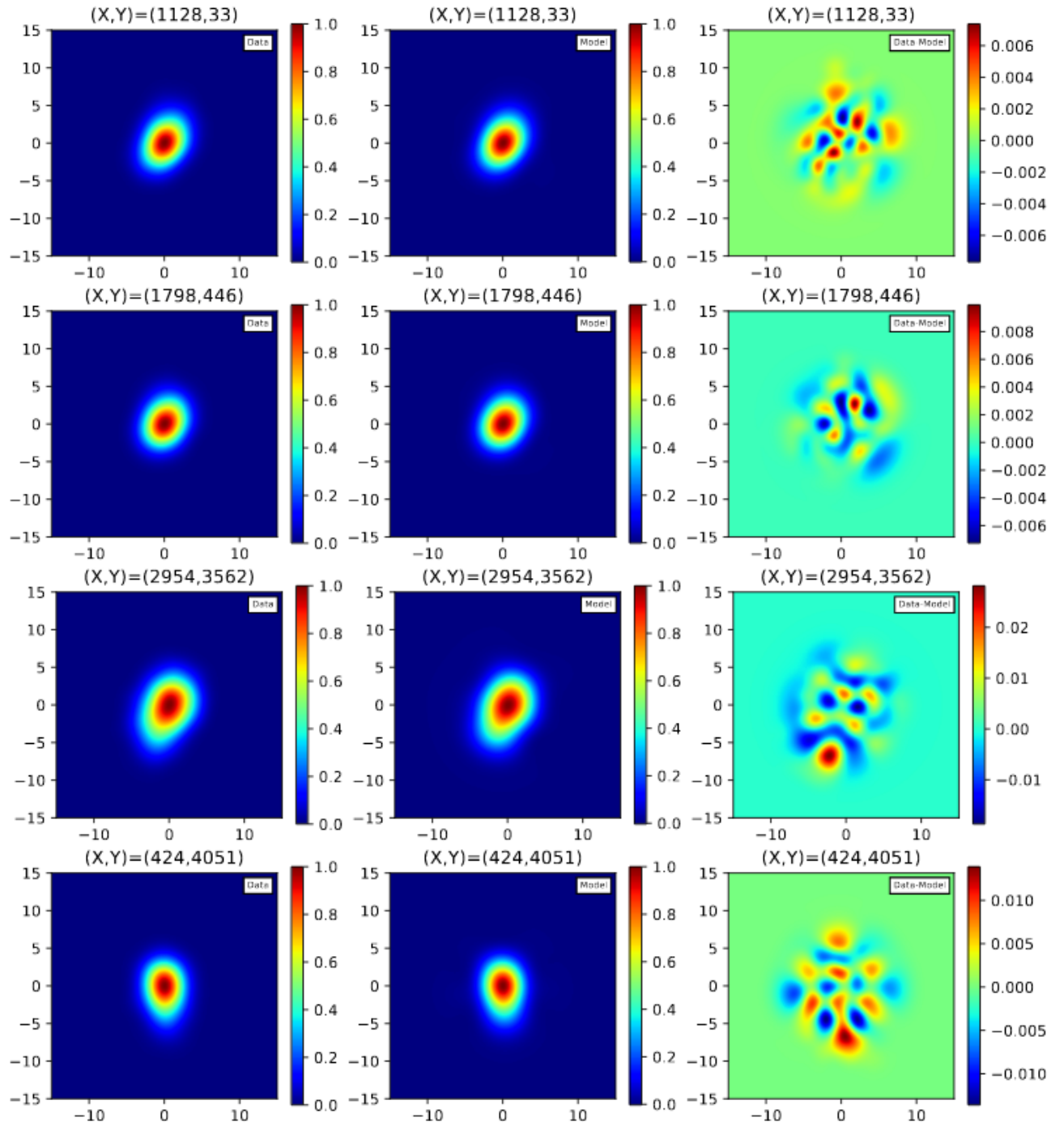


Figure 3.5: Some random star cutouts fitted with polar shapelets. The residuals are uncorrelated with the input PSF. X and Y at the top of the plots represent the PSF location on the CCD plane. Each image is plotted for x and y axis form  $-8$  to  $8$ , colorbar represents the photon counts.

# Chapter 4

## Photometry Error Analysis

### 4.1 PSF Photometry Error

With PSF models we can perform very high accuracy photometry. Error in photometry can be reduced to a large extent compared to aperture photometry. PSF photometry uses principles of linear template fitting to get the flux.

$$data = A \times PSF + B,$$

above equation is a matrix equation (flux is scalar) and should be true for all pixels in image, here data is the real star image and B is the uniform sky background. Sky background can be estimated very accurately from other means and star image can be flat fielded. Now we have,

$$data = A \times PSF, \quad (4.1)$$

summing both side gives,

$$photon\ counts = flux = A,$$

as PSF is normalized to unity. We need to get  $A$  from equation 4.1 to get the total flux of the star. Using least square fitting (fitting a straight line) we get following formula for  $A$  and  $\Delta A$ ,

$$flux = \frac{\sum_{i,j} PSF_{i,j} data_{i,j}}{\sum_{l,m} PSF_{l,m}^2}, \quad (4.2)$$

and

$$\Delta flux = \sqrt{\frac{\sum_{i,j} PSF_{i,j}^2 S_{i,j}^2}{(\sum_{l,m} PSF_{l,m}^2)^2}}, \quad (4.3)$$

here  $S_{i,j}$  is a element of sigma matrix, gives standard deviation of  $data_{i,j}$ . Generally  $S_{i,j}$  can be estimated using Poisson statistics (for photons) by  $\sqrt{data_{i,j}}$ . Above equations can be implemented in numpy(np) as some very simple array multiplication,

$$flux = np.sum(PSF * data) / np.sum(PSF ** 2),$$

$$\Delta flux = np.sqrt(np.sum(PSF ** 2 * S ** 2) / (np.sum(PSF ** 2)) ** 2).$$

In a simulation exercise, we verified the above flux and error formula. We created an ensemble of 10000 stars (given flux, drawn from Poisson distribution) of known PSF. The

mean and the standard deviation of the fluxes of the ensemble should be matching with the outcome of flux and error formula respectively. Distribution of fluxes is also observed to be Gaussian.

	$flux$	$\Delta flux$
Formula	175046	518.09
Gaussian Fit	175038	518.52

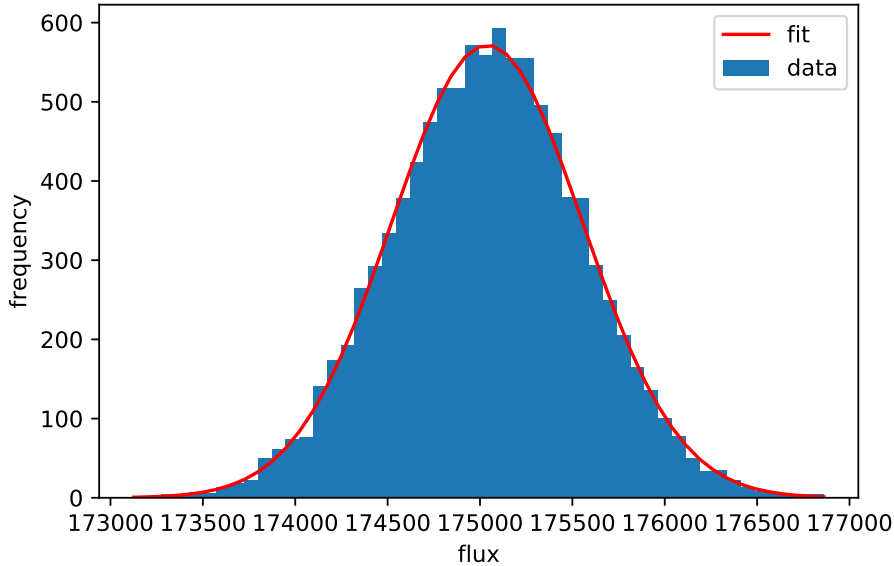


Figure 4.1: 1D Gaussian fitted with flux data.

## 4.2 Polar Shapelets PSF Photometry

### Background Estimation

We need to estimate the local sky background around each source using a nearby annulus aperture surrounding each source. The simplest method for doing so would be to perform photometry in an annulus aperture to define the mean(or other central tendencies) background level. In real life exposure, we observe numerous spikes in flat CCD, coming from various sources(like cosmic rays), making mean an inaccurate estimation of background. Alternatively, one can use aperture masks to directly access the pixel values in an annulus, and thus apply more advanced statistics. We calculated the sigma-clipped median within the annulus for the estimation of background as this method is immune to irregular spikes. In sigma clipped stats, we clip away data lying outside  $n$ -sigma( $n = 3$ , for our case).

The local background level around each source is estimated as the sigma-clipped median value within a circular annulus of inner radius 22 pixels and outer radius 27 pixels(keeping annulus far from source). The star image were subtracted with flat background image of same shape(see figure 4.2 ).

### Photometry

The following steps were taken to perform the Polar Shapelets PSF photometry for the Zemax output of WALOP.

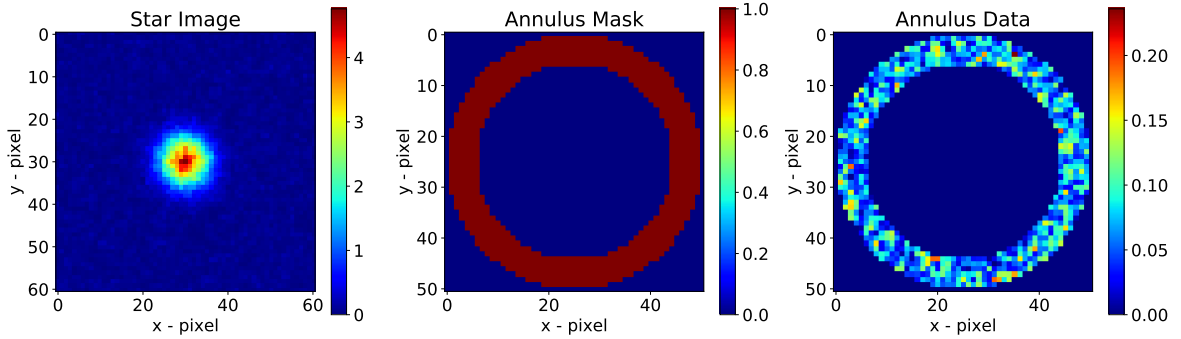


Figure 4.2: 1D Gaussian fitted with flux data.

- We created an input image( $4096 \times 4096$ ) with 400 stars on it. Stars were of specification mentioned in the last chapter. Stars were of magnitude 12 with a background of magnitude 20.
- Zemax simulation of WALOP processed the input image for the worst-case scenario.
- We made star cutouts from output image of Zemax (as in figure 2.7).
- We rolled each image in such a way that the maximum is at the center of the image.
- We estimated the background of each star and after flat fielding, created polar shapelets PSF model following steps mentioned in section 3.6.
- We used equations 4.2 and 4.3 to estimate photon counts and error in photon counts for each star.
- We plotted percentage error on CCD and histogram (see figure 4.3).

### 4.3 Error Analysis

In principle, any signal can be observed with the desired accuracy given enough exposure time. We too can control our percentage error with exposure time but at the same time, we also try to minimize our exposure time. The numbers of photons go linearly with the time(equation 3.3), but the error matrix goes with the square root on time.

$$S_{i,j} = \sqrt{N_{i,j}} \propto \sqrt{t},$$

here  $S_{i,j}$  error matrix and  $N_{i,j}$  is the number of photons on  $[i, j]$  pixel.

For 10 minutes of exposure time, we performed error analysis of photometry. We got an average percentage error of 0.16%. We plotted percentage error on CCD coordinates(see figure 4.3 ). We observed that we are able to do photometry at all area with an excellent accuracy(unlike figure 2.8).

With Polar shapelets PSF modeling, we accomplish the following advancements in photometric techniques.

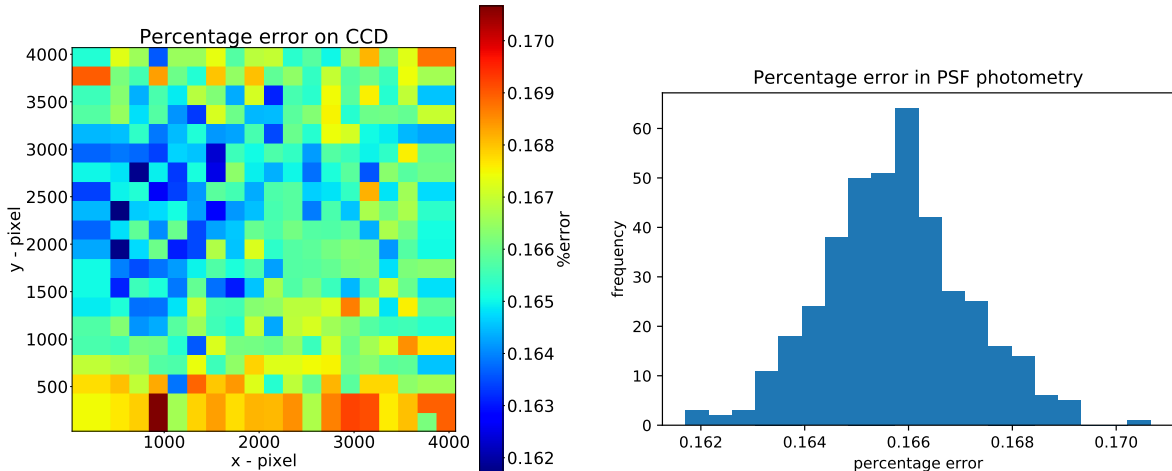


Figure 4.3: Left: Percentage error of PSF photometry on CCD. Right: Histogram of percentage error of PSF photometry of 400 stars.

- This is very simple to model and no fitting is involved (like curve fit or least square fit). This is also light in computation. For an optimized version of code, the whole process of modeling is just a few matrix multiplications.
- We can do PSF modeling of a wide field of view ( $30' \times 30'$ ) with includes other sub-instruments (like polarimeter).
- We can model very irregular PSF with ease and very accurately without going for brute polynomial fittings.
- We are also very close to achieving our desired accuracy for the PASIPHAE survey (which is 0.07%).

Our future plans are followings.

- We are still far from handling overlapped stars, as all of our exercises have been done by keeping stars away from each other. In real image, stars will be overlapped so we need to incorporate photometry of overlapped stars in our methods.
- With the development of a novel technique of PSF photometry, we also plan to contribute to the PSF photometry part of popular python module Photutils.
- We will also try to explore other applications of Polar Shapelet (and Cartesian Shapelet). One of the applications in image recognition we have presented in the next chapter.
- For our algorithm to work, we need to find a maximum of data roll maxima to center. This method might not be practical with sudden cosmic ray burst (unless we find a way to remove those). Another way is to work with the centroid of image (or other measures of central tendency). We may need to work on the centroid algorithm, which is used for finding the center of stars on the CCD image. Error in estimating centroid has the largest contribution in photometry error.

# Chapter 5

## Other Possible Applications of Shapelets Analysis

### 5.1 Image Components

In principle any 2D image can be expanded into polar shapelets, as polar shapelets are orthogonal and complete basis function (see equation 3.1 and 3.2). An optimized version of code is not more than just a few matrix multiplications and is far less time consuming than traditional brute curve fitting techniques. Recently the same technique has been implied into the study of the morphological classification of galaxy[19].

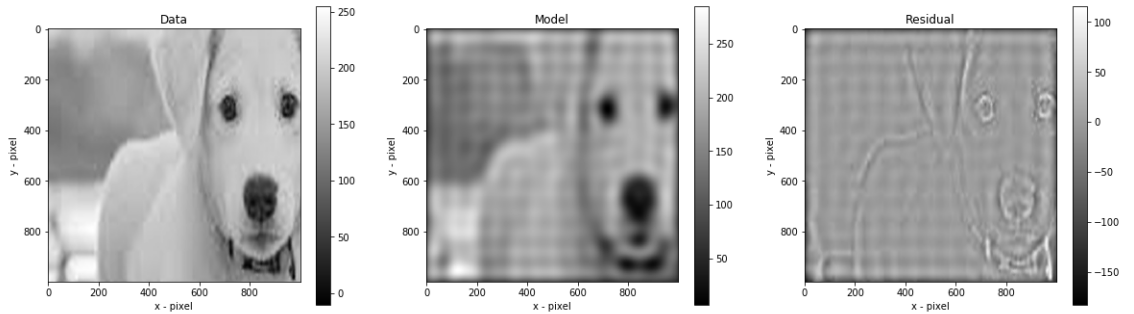


Figure 5.1: Recovering a black and white image of a puppy with polar shapelets analysis. It just needed 20 polar shapelets with a total of 231 components.

### 5.2 Application in Image Recognition

It has been observed that in polar shapelets (or Cartesian shapelets) analysis, the most natural features of an image are captured in the first few shapelets. The more shapelets we include, the finer features get captured. For example, most useful features of 100 pixels(total 10000 attributes for artificial neural network techniques) image, could be captured into just 231 variables(see figure 5.1). We downloaded a huge image(RGB) dataset of animals(animals are more spherically symmetric than vehicles) from [Kaggle](#). We tried some machine learning techniques along with the shapelet analysis to recognize images. We present results of our analysis in the next section.

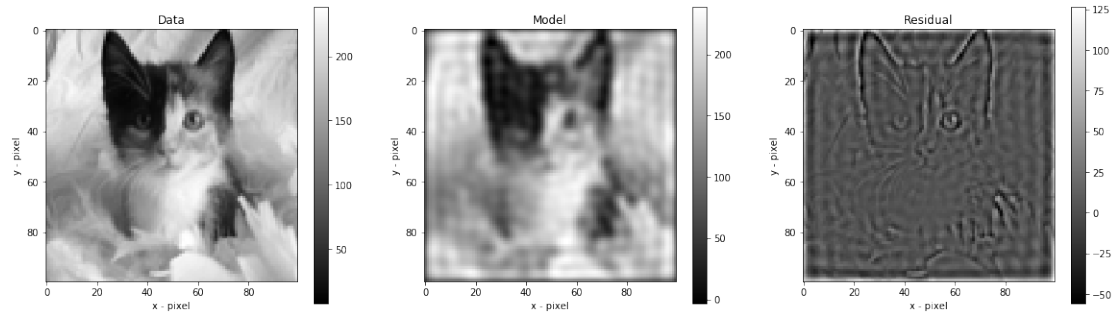


Figure 5.2: Component analysis of a low resolution black and white cat image( $100 \times 100$  pixels) with 20 polar shapelets .

### 5.3 Steps Taken

We need to clean and preprocess our data before feeding into machine learning algorithms. We fed shapelet components( $b_{n,m}$ ) instead of pixel values( $data_{i,j}$ ) data to our machine learning algorithm. Following steps were taken to train a machine learning algorithm to recognize images.

- Dataset, downloaded from Kaggle, contains a 1000 images of cat, dog and panda each, with a total of 3000 images(see some of sample figures 5.3, 5.4 and 5.5).
- Images were resize to  $100 \times 100$  pixel (see fig 5.2). Polar shapelets components were analyzed for each image with upto  $n = 20$ , a total of 331 components(gives a total of 662 features, because a complex number gives two variable). This saves a data matrix  $X(3000 \times 662)$  and a target array  $y$  containing labels(cat,dog and panda).
- In machine we are not able to operate with character, so we need to encode character label into some numbers. Simple encoding can be like cat:0, dog:1, panda:3, but this give a wrong impression to algorithm about the hierarchy of labels(like panda>dog as 3 > 2). We bypass this by using one hot encoder, like cat:[1,0,0], dog:[0,1,0], panda:[0,0,1].
- Data were divided into training(80%) and test(20%) sets.
- Many machine learning classifiers (SGD Classifier, Random Forest Classifier, K-neighbor Classifier, Support Vector classifier, and ANN Classifier ) were trained with training data and tested with test data.

cats

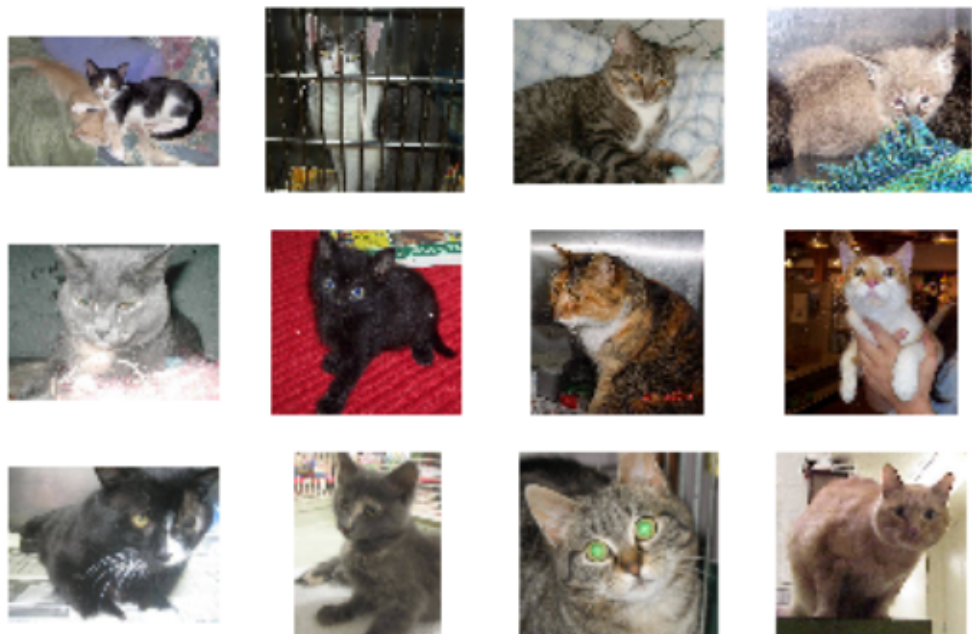


Figure 5.3: Some sample image of cats from the datasets.

dogs

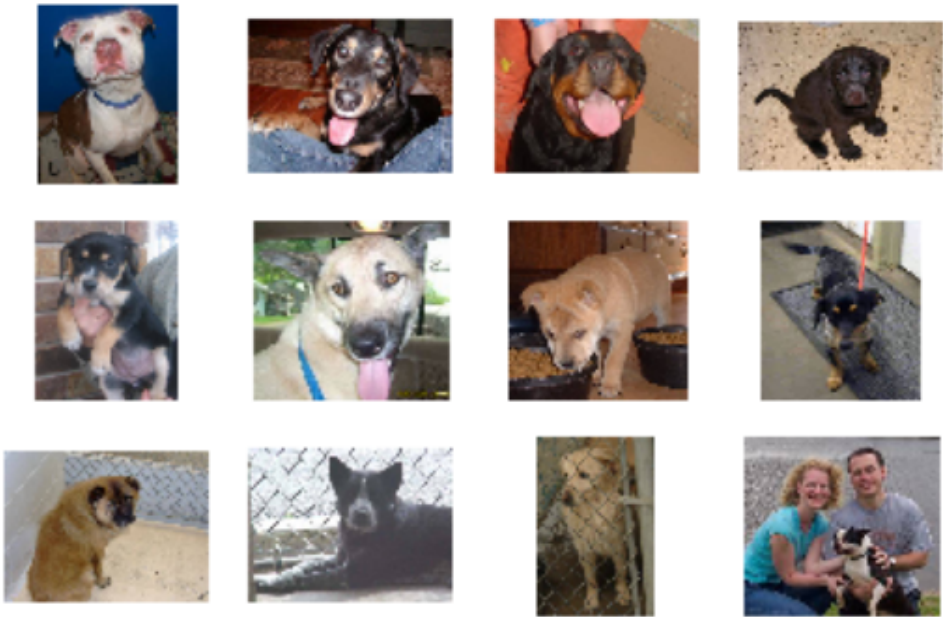


Figure 5.4: Some sample image of dogs from the datasets.

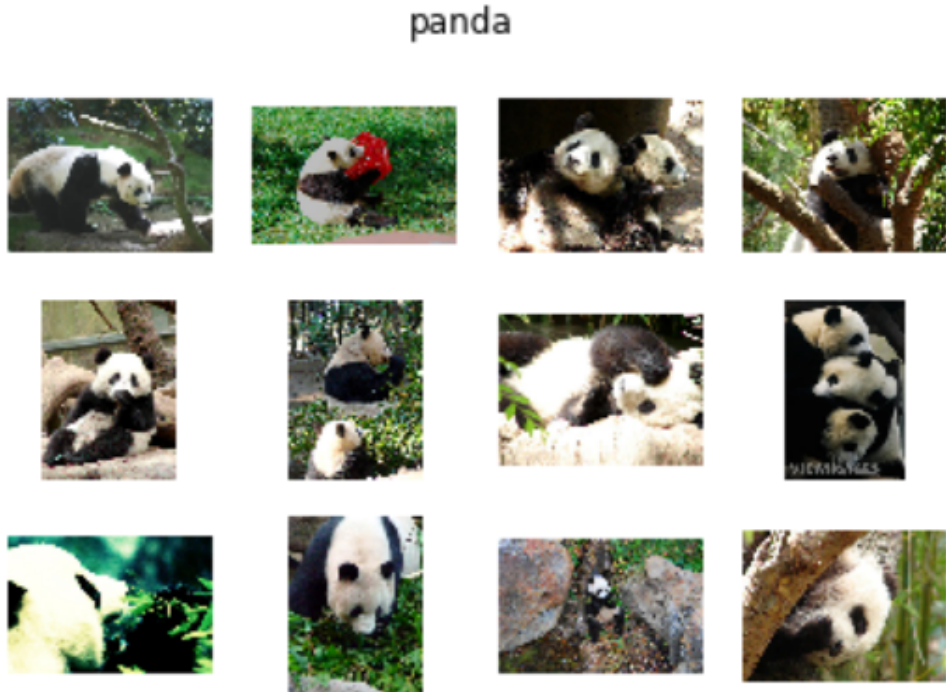


Figure 5.5: Some sample image of pandas from the datasets.

## 5.4 Results

Accuracy of classification techniques can be measured in terms of precision and recall. We analyzed the prediction accuracy of machine learning algorithms using the confusion matrix and the F-score. Here we present the best result produced by the Random Forest Classifier.

### Precision

The precision of a classification algorithm is defined as,

$$\text{precision} = \frac{\text{true positives}}{\text{true positives} + \text{true negatives}}$$

here true positives are positive labels predicted as positive and true negatives are positive labels predicted as negative.

### Recall

Recall of a classification algorithm is defined as,

$$\text{recall} = \frac{\text{true positives}}{\text{true positives} + \text{false negatives}}$$

here false negatives are positive labels predicted as negative.

## F-score

Usually, it is not possible to keep both the above metric healthy. We trade-off between above according to our needs. A single metric F-score is the harmonic mean of precision and recall.

$$F\text{-score} = \frac{2}{\frac{1}{precision} + \frac{1}{recall}}$$

The above measurements are defined for binary classes but can be successfully extended to the multi-class system by taking an average of scores of one vs all at a time.

We got F-score for our trained algorithm to be 0.68 and the confusion matrix has been shown in figure 5.6. In the future, we can deploy the following techniques to improve our results,

- As we have analyzed only black and white images, our algorithm was not able to look into the colors of the animal(which are important features of the animal, I guess). We can use RGB data of the image to train the algorithm for further improvement.
- As we can see figure 5.4, many images are contaminated with other objects(like humans), giving wrong signals to the algorithm. We can clean images for further improvements.
- We only had 3000 data sets, not enough to fit hyper-parameters of algorithms. We plan to access a huge dataset to check the polar shapelet technique.

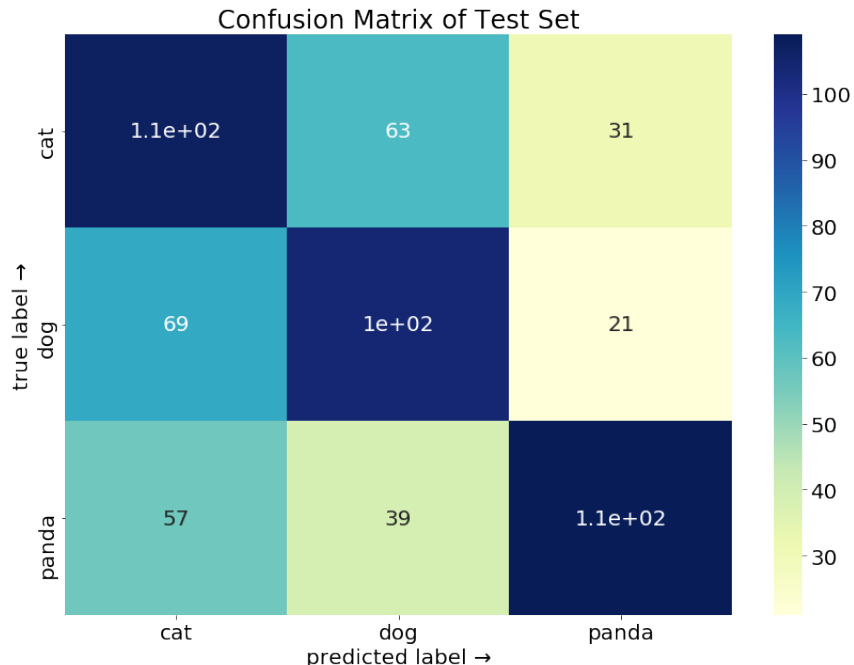


Figure 5.6: Confusion matrix for predicted class by the Random Forest Classifier. Element  $[i, j]$  represent number on instance algorithm confused  $i^{th}$  label for  $j$ . For example element [1, 2] is number of cases algorithm confused a cat for a dog

# References

- [1] POLARIZED LIGHT AND THE STOKES PARAMETERS <http://astrowww.phys.uvic.ca/~tatum/physopt/physopt4.pdf>
- [2] Wollaston Prism [https://en.wikipedia.org/wiki/Wollaston\\_prism](https://en.wikipedia.org/wiki/Wollaston_prism)
- [3] "Wollaston prism". AMS Glossary. Retrieved 2013-04-29.
- [4] RoboPol: A four-channel optical imaging polarimeter <https://arxiv.org/abs/1902.08367>
- [5] PASIPHAE: A high-Galactic-latitude, high-accuracy optopolarimetric surve <https://arxiv.org/pdf/1810.05652.pdf>
- [6] The WALOP polarimeters <http://pasiphae.science/walop>
- [7] The RoboPol Pipeline and Control System <https://arxiv.org/pdf/1310.7555.pdf>
- [8] <https://cmb-s4.org/>
- [9] POLARBEAR-2: an instrument for CMB polarization measurements<https://arxiv.org/abs/1608.03025>
- [10] <https://cmb-s4.org/>
- [11] Seeing Measurements at Skinakas Observatory using the DIMM method<https://arxiv.org/abs/astro-ph/0111022>
- [12] Tassis, K., Pavlidou, V. 2015, MNRAS,451, L90
- [13] A good read for Photon statistics and sky noise. <http://slittlefair.staff.shef.ac.uk/teaching/phy217/lectures/instruments/L14/index.html>
- [14] Why PSF fitting?[http://web.ipac.caltech.edu/staff/fmasci/home/astro\\_refs/WhyPSFFit.pdf](http://web.ipac.caltech.edu/staff/fmasci/home/astro_refs/WhyPSFFit.pdf)
- [15] Algorithms of CCD photometry.<https://www.adass.org/adass/proceedings/adass98/mighellkj/>
- [16] Daophot <https://ui.adsabs.harvard.edu/abs/1987PASP...99..191S/abstract>
- [17] Building an EPSF. <https://ui.adsabs.harvard.edu/abs/2000PASP..112.1360A/abstract>
- [18] Zernike polynomials fitting idea. <https://arxiv.org/abs/1302.0145>
- [19] Using polar shapelets technique in morphological classification of galaxy. <https://arxiv.org/pdf/astro-ph/0408445.pdf>